



Université  
de Toulouse

# THÈSE

En vue de l'obtention du

## DOCTORAT DE L'UNIVERSITÉ DE TOULOUSE

Délivré par : *l'Institut National Polytechnique de Toulouse (INP Toulouse)*

---

---

Présentée et soutenue le JJ/MM/2018 par :

**NICOLA LUMINARI**

---

Le titre de la thèse

---

---

### JURY

PREMIER MEMBRE

Professeur d'Université

Président du Jury

SECOND MEMBRE

Astronome Adjoint

Membre du Jury

TROISIÈME MEMBRE

Chargé de Recherche

Membre du Jury

---

École doctorale et spécialité :

*MEGEP : Dynamique des fluides*

Unité de Recherche :

*Institut de Mécanique des Fluides de Toulouse (I.M.F.T.)*

Directeur(s) de Thèse :

*M. Alessandro BOTTARO et M. Christophe AIRIAU*

Rapporteurs :

*Premier RAPPORTEUR et Second RAPPORTEUR*

# Contents

<b>1 Poroelastic natural coatings</b>	<b>8</b>
1.1 Biomimetics of poroelastic coatings . . . . .	8
1.1.1 Riblets and shark-skin surfaces . . . . .	11
1.1.2 Permeable surfaces . . . . .	16
1.2 Models for flows through porous surfaces . . . . .	19
1.2.1 Drag that is function of the canopy depth (canopy flow, flow vegetation) . . . . .	19
1.2.2 Porous media approach through homogenization . . . . .	19
1.3 Stability of flow over permeable surfaces (monami and honami) . . . . .	19
1.3.1 Stability theory generalities . . . . .	19
1.3.2 Monami Honami . . . . .	19
<b>2 Volume Average Navier-Stokes Equations</b>	<b>20</b>
2.1 Introduction . . . . .	20
2.2 Derivation of VANS equations for 3D incompressible fluids . . . . .	20
2.2.1 Definition of the averaging filter . . . . .	20
2.2.2 Theorems involving derivatives of spatial averaging . . . . .	22
2.2.3 Length scale decomposition . . . . .	22
2.2.4 Averaged continuity equations . . . . .	22
2.2.5 Averaged momentum equations . . . . .	22
<b>3 Drag-model sensitivity of Kelvin-Helmholtz waves in canopy flows</b>	<b>23</b>
3.1 Introduction . . . . .	23
3.2 Model of the canopy flow . . . . .	24
3.2.1 The mean flow . . . . .	24
3.2.2 Stability and sensitivity equations . . . . .	27
3.3 SENSITIVITY RESULTS FOR THE ISOTROPIC DRAG MODEL . . . . .	29
3.4 AN ALTERNATIVE SENSITIVITY MODEL: ACCOUNTING FOR THE CANOPY ANISOTROPICITY . . . . .	32
3.4.1 The sensitivity equations . . . . .	33
3.5 CONCLUDING REMARKS . . . . .	35

<b>4 Effect of geometrical parameters and inertia on the apparent permeability tensor in fibrous porous media</b>	<b>42</b>
4.1 Introduction . . . . .	42
4.2 The Volume-Averaged Navier-Stokes (VANS) method . . . . .	45
4.3 Validation and setup . . . . .	45
4.3.1 Computational domain . . . . .	45
4.3.2 Numerical setup . . . . .	46
4.3.3 Mesh convergence analysis . . . . .	46
4.3.4 Validation on two different configurations . . . . .	48
4.3.5 Tests with larger REV's . . . . .	48
4.4 Microscopic solutions . . . . .	50
4.5 The apparent permeability tensor . . . . .	57
4.6 A metamodel for $\mathbf{H}$ . . . . .	61
4.6.1 DACE sampling . . . . .	62
4.6.2 Kriging interpolation method . . . . .	65
4.7 Concluding remarks . . . . .	68

# List of Figures

1.1	Microscope enlarged picture of the shark skin. . . . .	9
1.2	Feathers in owl's wing: trailing edge (left), leading edge (right). The difference in shape, and mechanical properties as rigidity, between the leading and trailing edge is a consequence of the different flow regimes in the wing.	9
1.3	Peacock butterfly wing surface using Scanning Electron Microscopy. Images from wikimedia.org . . . . .	10
1.4	(a) Scanning electron microscopy (SEM) image showing the structure of lotus leaf, (b) higher order of magnification on the single protuberance forming the surface and (c) a water drop that due to the contact angle attain an almost spherical shape. Images from [67] . . . . .	11
1.5	Schematics of the concept of <i>protusion height</i> . The mean velocity profiles for the streamwise and crossflow velocities are presented. Where they are in the presence of a ridge is it possible to extrapolate the point of zero velocity from the velocity gradient outside the riblet, finding respectively the <i>streamwise protusion height</i> $h_{ps}$ and the <i>crossflow protusion height</i> $h_{pc}$ . Image from Bechert et al. [10] . . . . .	12
1.6	Performance ... Jimenez et al. [43] . . . . .	13
1.7	Two different size of riblets are represented interacting with a sublayer vortex. In grey is it represented the areas where the friction is important; clearly when the size of two is comparable (as the left picture) the surface experience a larger friction and the performance is lowered. Image from Choi et al. [25] . . . . .	13
1.8	$DR\% = \frac{\Delta\tau}{\tau_0}\%$ Image from Itoh et al. [41]. . . . .	15
1.9	Diagram showing an example of pressure distribution around a cylinder for a viscous flow. The black line is the angular distribution as a solid body, the green one is the modified pressure in presence of a porous layer at the rear part. Image from Klausmann and Ruck [44] . . . . .	17
1.10	Square cylinder vorticity countour for $Re = 30000$ . Top: solid case. Bottom: porous case with layer extension $h = 10\%D$ . . . . .	18

2.1	Illustration of the REV concept. . . . .	21
3.1	Configuration studied with main notations . . . . .	25
3.2	Left frame: mean flow $U$ , together with experimental data points [35], its first derivative, and drag coefficient distribution (case G). Center: viscous and inviscid growth rates, $\omega_i$ , as a function of the streamwise wavenumber $\alpha$ . Right: corresponding frequencies, $\omega_r$ . . . . .	26
3.3	Moduli of direct (left frame) and adjoint (right frame) eigenfunctions for the viscous (continuous lines, $Re = 3450$ ) and the inviscid (symbols) case, in correspondence to the wavenumber of largest amplification. . . . .	28
3.4	Real and imaginary parts of the sensitivities to mean flow variations (top) and to variations in the drag distribution function (bottom), for the parameters of 3.3 . . . . .	30
3.5	Infinite norms of the sensitivity functions for varying $\alpha$ . . . . .	31
3.6	Amplification factor (left) and frequency of the most unstable mode as a function of $\alpha$ , for the anisotropic drag model . . . . .	33
3.7	Left and center frames: moduli of direct and adjoint eigenfunctions; pressure and “adjoint pressure” are drawn with dashed lines. Right: real and imaginary parts of the sensitivity function $G_U$ ( $\alpha = 0.4790$ ) . . . . .	34
3.8	Case G. Left: infinite norm of $G_U$ for varying $\alpha$ . Center and right frames: real and imaginary parts of the sensitivity coefficients to variations in the permeability components . . . . .	35
3.9	Case G. Left: mean velocity profile, $U$ , versus the drag coefficient, $C_d$ . Right: first derivative, $dU/dC_d$ . The triangles denote the region $y \in [0.76, 1]$ , the filled circles denote the region $y \in [0.3, 0.76]$ . . . . .	37
4.1	REV for the fiber geometry investigated. . . . .	45
4.2	Mesh used for the computation; top view (left) and zoom in the boundary layer region (right). $\varepsilon = 0.6$ . . . . .	47
4.3	Permeability versus porosity for a square arrangement of cylinders. The scaling of the permeability is $\ell^2$ and is explicitly indicated in the vertical axis. . . . .	49
4.4	Permeability versus porosity for a staggered arrangement of cylinders. The permeability component is here scaled with $d^2$ (and not $\ell^2$ ), with $d$ the diameter of the inclusions. . . . .	50
4.5	Relative error between the microscopically computed forces along the $x_1$ direction and those arising from the Darcy-Forcheimier model; $\varepsilon = 0.8$ for the REV in the staggered arrangement of Yazdchi et al. [71]. . . . .	51
4.6	REV configurations. Left: $2 \times 2 \times 1$ arrangement; centre: $1 \times 1 \times 1$ arrangement (reference); right $1 \times 1 \times 3$ arrangement. . . . .	51

4.7	Top row: plane view of the dimensionless $x_1$ component of the local velocity field $\mathbf{v}_\beta$ for the case $\theta = 0, \phi = 0, \varepsilon = 0.6$ and for three Reynolds numbers $Re_d = 0, 10, 50$ , from left to right. Mid row: microscopic $M_{11}$ fields corresponding to the images in the top row. Bottom row: $M_{11}$ fields for the same Euler angles and Reynolds number as in the top two rows, and smaller porosity ( $\varepsilon = 0.4$ ). . . . .	53
4.8	right: Non-dimensional $M_{21}$ field for $\theta = 0, \phi = 0, Re_d = 10, \varepsilon = 0.8$ , left: Non-dimensional $M_{12}$ field for $\theta = 22.5^\circ, \phi = 45^\circ, Re_d = 50, \varepsilon = 0.4$ . . . . .	54
4.9	Non-dimensional $\mathbf{M}$ components fields for the case $\theta = 22.5^\circ, \phi = 45^\circ, Re_d = 50, \varepsilon = 0.6$ . . . . .	56
4.10	Diagonal elements of the apparent permeability $\mathbf{H}$ as function of the Reynolds number for porosity $\varepsilon = 0.8$ . The forcing direction is represented through the couple of Euler angles $(\theta, \phi)$ (cf. table 4.2 for the case index). Left column: low- $Re_d$ regime; right column: inertial regime. . . . .	58
4.11	Same as figure 4.10 with porosity $\varepsilon = 0.6$ . . . . .	59
4.12	Same as figure 4.10 with porosity $\varepsilon = 0.4$ . . . . .	60
4.13	Scatter matrix plot for the collected numerical data of the apparent permeability tensor. . . . .	63
4.14	Explanatory sketch for the relation between mean pressure gradient and mean velocity field. . . . .	64
4.15	Response surfaces of $H_{11}$ with $\phi = 0^\circ$ for porosity $\varepsilon = 0.4, 0.6, 0.8$ , from left to right. . . . .	67
4.16	Response surfaces of $H_{11}$ with $\theta = 0^\circ$ for porosity $\varepsilon = 0.4, 0.6, 0.8$ , from left to right. . . . .	68
4.17	Response surfaces of $H_{11}$ with $Re = 40$ for porosity $\varepsilon = 0.4, 0.6, 0.8$ , from left to right. . . . .	69
4.18	Response surface of $H_{11}$ ; in the left frame $\phi = \theta = 0$ , in the centre frame $\phi = 90^\circ, \theta = 0$ and on the right $\phi = 45^\circ, \theta = 22.5^\circ$ . . . . .	70

# List of Tables

3.1	Temporal versus spatial stability, Case G. The model employed here is based on a modified Orr-Sommerfeld equation—rather than a system based on primitive variables as done in the bulk of the paper—which is why the temporal results have slightly larger growth rates $\omega_i$ than those displayed in Fig. 3.2; this is related to the need of computing numerically $d^2U/dy^2$ and $dC_d/dy$ in the Orr-Sommerfeld-like equation. In italics, the growth rates obtained from Gaster’s transformation are reported; the parameters imposed in each simulation are indicated with bold characters. The solutions for $Re = 10^9$ coincide with those found using the inviscid equations. . . . .	39
4.1	Convergence analysis. Left: average velocity within the REV, normalized with $\frac{K_{11}}{\nu_\beta} \ \mathbf{f}\ $ . Right: grid convergence metrics. The REV has $\varepsilon = 0.6$ , the motion is along $x_1$ , i.e. $\theta = \phi = 0$ and $Re_d \rightarrow 0$ . . . . .	48
4.2	Directions of the forcing tested and property of the solutions. . . . .	57
4.3	Sampling parameters. . . . .	62
4.4	Permeability components ratio for three values of the porosity. The permeability ratios here are given by the angular coefficients of the linear correlations displayed in figure 4.13. . . . .	65

# Chapter 1

## Poroelastic natural coatings

### 1.1 Biomimetics of poroelastic coatings

Usually when someone is asked to imagine some "rapid" object as an airplane, a boat or a car, the common sense lead us to think about it as the smoothest as possible and most of the time shiny. But if we look around us the nature seems not to agree with the previous statement. In fact most of the surfaces in nature are not smooth at all, they present almost always some kind more or less regular arrangement of discontinuities at various length scales. Since Nature have had a very large time-span to optimize this kind of surfaces we can be very certain that they are the best possible option. One should pinpoint that the non smoothness of these surfaces can be connected to some other biological functions rather than pure fluid dynamic performance, and of course it can be the case.

With that in mind we want to show to the reader some of the most notably examples of "natural" aerodynamically surfaces.

Probably the most notable example is the shark skin, in figure 1.1 a segment of the skin is depicted as if appears to be under the microscope.

The enlargement show that the surface is made up by a series of overlapped denticles, and experiment shows that they can move and interact with the flow.

The shark technology has somehow been applied by Speedo® in their famous swimming suits, that had break multiples world records. But it seems that this controversial swimmers performance came more on the compressed and streamlined body shape than from the surface texture itself. In fact during the years this texture material has been publicized to be like synthetic shark skin but [57] has shown that the texture is somehow different from the shark dermal structure. They have also performed some swimming experiment with a flat plate with different surfaces and they have found no significant speed enhancement with the swimsuit surfaces; but the measurements with the shark skin on the contrary give an appreciable improvement in the performance.

Poroelastic surfaces find also applications in aeroacoustics, in fact the owl is well known

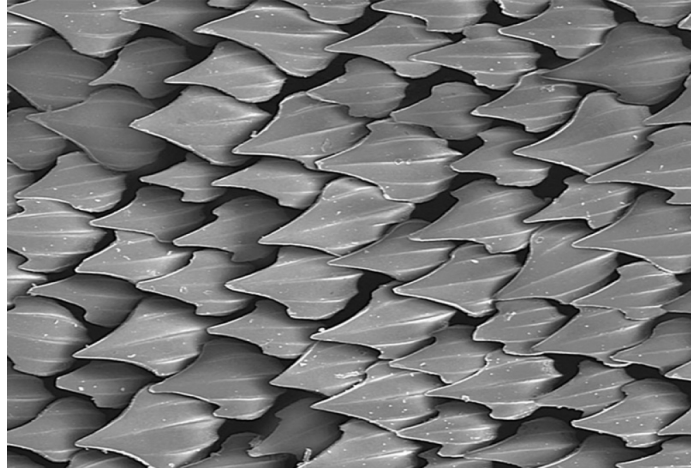


Figure 1.1: Microscope enlarged picture of the shark skin.

for its particularly silent flight, in the high frequency spectrum. This characteristic is crucial for the owl in order to be able to capture his preys. Obviously it has inspired the scientific community to study the feathers configuration and their shape.



Figure 1.2: Feathers in owl's wing: trailing edge (left), leading edge (right). The difference in shape, and mechanical properties as rigidity, between the leading and trailing edge is a consequence of the different flow regimes in the wing.

Multiple authors show promising result in characterizing the acoustic properties of the owl skin and their physical mechanism. In particular [50] present three main characteristic of the owl that can suppress its airborne noise: the feathers leading edge shaped like a comb, the feathers trailing edge that form a fringe and the presence of multiple "filaments" in the bottom surface of the wing and on its legs. in the same work he also present some experimental and empirical evidence on the aeroacoustics mechanism behind the three elements above.

Another examples of work in the field of owls acoustic is the one by [42] in which the authors study the acoustic scattering problem of a poroelastic half-plane hit by an

incident plane wave. This configuration has been used as an analogy with the owl wing, it try to explain how the properties of this surface can suppress the noise. They conclude that the combined effects of elasticity and porosity can produce the weakest edge noise amplification.

Recent computational simulation made by [24] confirm that the leading edge shape of the feathers truly suppress noise and enhance the lift generation for angles of attack grater then  $15^\circ$ .

Bioinspired aerodynamic surfaces include another peculiar example in the butterflies wings. In figure 1.3 the surface of a "Peacock butterfly" is enlarged in order to show the multiple scales involved; the wing structure present firstly as overlapped scales similar to the shark, but looking closely we can observe that the singles scales have a complicated permeable structure.

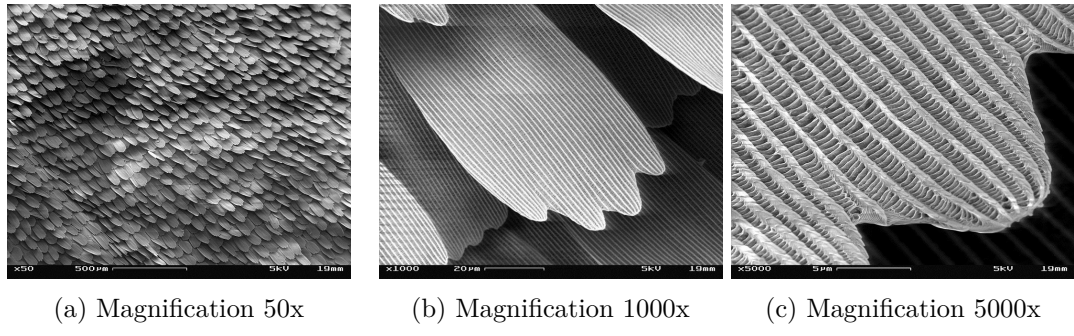


Figure 1.3: Peacock butterfly wing surface using Scanning Electron Microscopy. Images from [wikimedia.org](#)

The work of Slegers et al. [64] the authors study the effect of such porous structure in the flight performance of butterflies. Using cameras to measure the kinematics of their flight, they can compute their efficiency to "climb" (generate lift) and the stroke amplitude and frequency. The authors conclude, after the proper statistical tests on the overall butterfly population, that the porous structure of their wing gives a boost in climbing efficiency about 30%; that results clearly stress out the importance of the poroelastic layer of the wings. Even though the flight aerodynamic is extremely complex [66], it seems clear that the peculiar structure of the wings surface is critical for their aerodynamic performances.

Superhydrophobic surfaces works as they were water repellent, in fact over such surfaces the water can slide over with much less resistance resulting in very small values of wettability. This behavior is caused by the microscopic structure that forms the surface 1.4, in fact the rugosities are arranged in a more or less regular way in order to be able to capture air pockets that rest inside this structures. These air inclusion provoke an effective slip at the air-liquid interface that cause the drag reduction; but they also change the contact angle of droplets The work of Bottaro et al. [14] summarize the above aspect and

their applications.

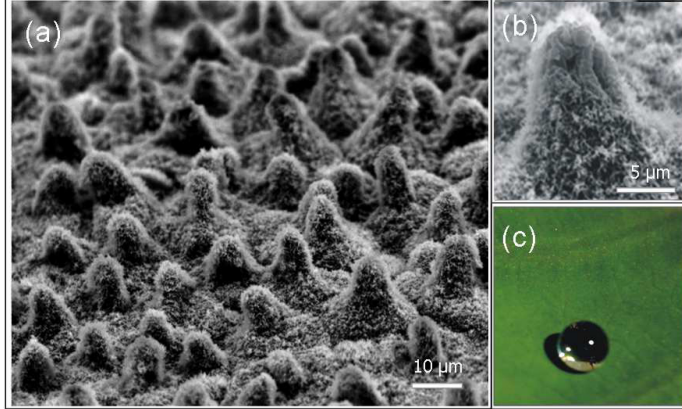


Figure 1.4: (a) Scanning electron microscopy (SEM) image showing the structure of lotus leaf, (b) higher order of magnification on the single protuberance forming the surface and (c) a water drop that due to the contact angle attain an almost spherical shape. Images from [67]

The interest reader could find other examples and broaden the above key aspect also in [12], [68].

### 1.1.1 Riblets and shark-skin surfaces

We have seen that natural surface can be an inspiration to find strategies to solve many aerodynamics problems; in the following we will focus especially on the drag reduction.

Is known that the total drag contribution can be separated in different components, and the classical decomposition is between viscous drag (sometimes referred as skin friction) and pressure drag.

$$\int_{A_\sigma} \left[ \underbrace{\left( \frac{p}{\rho} \mathbf{I} \right) \cdot \mathbf{n}_\sigma}_{\text{pressure drag}} + \underbrace{(\nu \nabla \mathbf{v}) \cdot \mathbf{n}_\sigma}_{\text{viscous drag}} \right] dA, \quad (1.1)$$

Where  $A_\sigma$  is the solid interface of some body where a no slip condition is applied, and  $\mathbf{n}_\sigma$  is its outward normal. In this section we will talk about the existing possible ways to reduce the viscous part of the drag since historically has attract more interest and/or make more progress.

In the following we will refer as the wall shear stress in the turbulent case as:

$$\tau = ((\mu + \mu_t) \nabla \bar{v}) \cdot \mathbf{n}_\sigma = (\mu + \mu_t) \frac{\partial \bar{u}}{\partial y} \quad (1.2)$$

where  $\mu_t$  is the turbulent viscosity and  $\bar{u}$  is the average velocity streamwise component; in the laminar case obviously the definition rest the same with some correction (there is no turbulent viscosity and no notion of average velocity). Also  $\mathbf{n}_\sigma = (0, 1, 0)$  is the conventional orientation in the literature.

Most of the industrial application involves turbulent flow; obviously there is a lot of research that aim to reduce the skin-friction in this regime. Table 6.3.1 in the book of McLean [53] make a wide list of technique already been proposed on the problem.

As the same author pinpoint the most effective, and probably the most practicable concept, are the riblets. They are regularly arranged alternating ridges aligned in the streamwise flow direction as the figure 1.5 show.

These surfaces are capable of align the turbulent flow in the mean flow direction smoothing the fluctuation of the cross-flow in the viscous sublayer. Reducing this fluctuations close to the surface the turbulent momentum transfer will also be reduced and so the shear stress, causing the reduction in skin-friction.

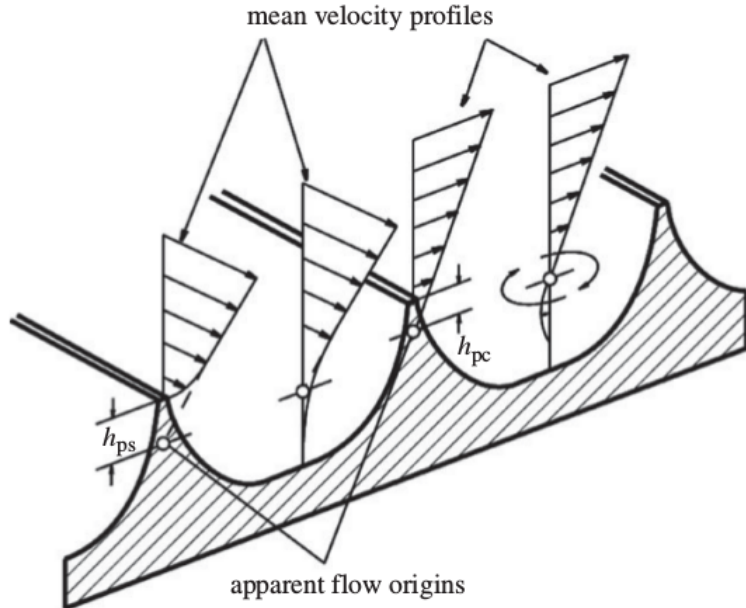


Figure 1.5: Schematics of the concept of *protusion height*. The mean velocity profiles for the streamwise and crossflow velocities are presented. Where they are in the presence of a ridge is it possible to extrapolate the point of zero velocity from the velocity gradient outside the riblet, finding respectively the *streamwise protusion height*  $h_{ps}$  and the *crossflow protusion height*  $h_{pc}$ . Image from Bechert et al. [10]

The viscous drag reduction correlates well with the spacing between the ridges expressed in wall units  $s^+$ , the typical shape is depicted in 1.6 where the vertical axis show the drag

reduction computed against the smooth surface case against the  $s^+$ . This general shape of the curve, in which the skin friction decrease in certain range of spacing and then increase as the  $s^+$  increase, is caused by a competition between the capacity of riblets to obstruct lateral fluid flow and an increase in the penetration of high speed vortices inside this manufactured rugosities.

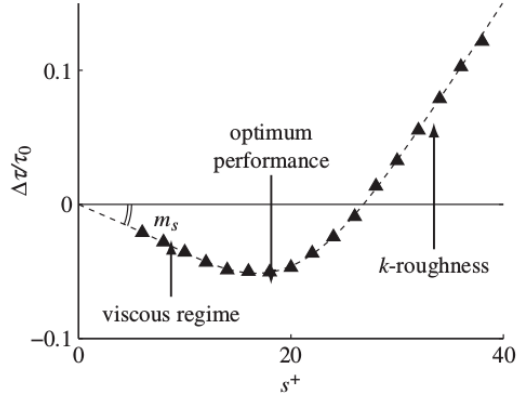


Figure 1.6: Performance ... Jimenez et al. [43]

This last physical explanation of the riblets performances is presented in the schematics 1.7, where the grey areas show high skin-friction regions caused by the downwash motion generated by the near-wall vortices. Is it clear that when the riblets are too big the vortices can penetrate inside its groove and actually increase the skin-friction due to larger area exposed to the local velocity. On the contrary when the riblets are smaller, the high speed vortices "touch" only the tip of the ridges so only a small local area of the surface experience high-shear stresses.

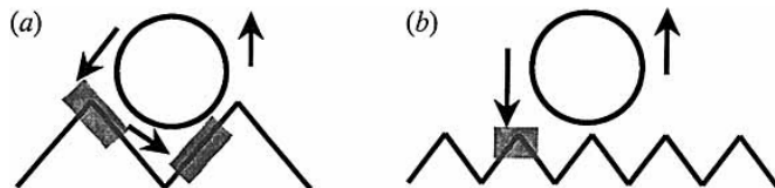


Figure 1.7: Two different size of riblets are represented interacting with a sublayer vortex. In grey is it represented the areas where the friction is important; clearly when the size of two is comparable (as the left picture) the surface experience a larger friction and the performance is lowered. Image from Choi et al. [25]

The slope  $m_s$  of the curve 1.6 can be predicted by linear stability theory or by means

of empirical correlations as in García-Mayoral and Jiménez [34].

Computing the performance of such surfaces can be expensive since the most reliable quantitative theory for such problems are DNS simulations or experiments. There is only one other theory, besides the already cited expensive ones, that use the concept of *protusion height* showed in 1.5 to correlates the shape of the protusion to the drag reduction Luchini et al. [51]. The *protusion height* is defined as the vertical distance between the riblet top ridge and point of zero velocity extrapolated from the constant velocity gradient outside above the protusions. It seems that especially the difference of protusion heights computed from the streamwise  $h_{ps}$  and cross-flow flow  $h_{pc}$  correlates very well with the drag reduction, and the two quantities can be computed with a simple Stokes problem over the local geometry of the grooves.

Another very impressive characteristic is that the performance are robust in off-design, such as the yaw (misalignment between the flow and the riblets ridges) and tip erosion of the ridges García-Mayoral and Jiménez [33].

But still besides some very specific application, such as sailing competitions in which the hulls of the USA challengers in the America's Cup 1987 and 2010 were fitted with riblets, the massive utilization of this technology is still in question. Since the riblets size need to be very little, producing such surfaces in a larger area like the roof of a car or the wing of an airplane can be an issue for a routine use.

Riblets like surface has been observed in nature for many years, for example Martin and Bhushan [52] found out that skimmer birds (*Rynchops*) have riblets like grooves in their beak, since they fly with it under the surface of the water to catch fishes. But, as already introduced, the most clear example of such natural surfaces are shark skin. In his review Dean and Bhushan [27] present the status of the shape optimization that has been done on the riblets trying to mimic the typical sawthooth shape seen in shark skin, showing that improvements of such geometries over the classical ones has yet to be proven. Shape optimization on riblets geometry has been studied also by Bechert et al. [10] finding that the drag reduction can be improved very little just working on the geometry even though a few % can be gained.

There is in fact some controversial result in literature that state that surfaces with actual shark skin replica can indeed increase drag. Boomsma and Sotiropoulos [13] for example perform some simulations on actual shark skin denticles using the immersed boundary method; he find that in some configuration the actual drag increase up to 40%, but even though the numbers are probably too large (it is know that the immersed boundary method can generate large errors in force computation especially in high Reynolds number flows), this can prove that the shark skin does not work with the same mechanism as riblets.

In fact Bechert et al. [9] had already tested such geometries in his experiments. He builds a synthetic surface made by artificial shark denticles posed on top of spings and he measure that even with the introduction of the surface elasticity the actual drag was increasing. however the authors pinpoints that the actual shark flow regime is nothing at all as steady as the experiments that he performed, and he speculates that the excellent

swimming performance of the shark came from the separation control that flexible denticles can increase in the periodic oscillating flow that the swimming generate.

Experiment using DPIV on a NACA covered with actual skin samples of "Isurus oxyrinchus" mako shark, has been performed by Lang et al. [47], confirming that the flexibility of sharks denticles perform as a passive flow control in order to avoid early separation. In fact the experiments proves that for angles of attack larger than  $15^\circ$  the flow reversal is almost completely avoided. The same author introduce the importance in the different geometries of the denticles in different part of the body that obviously experience different flow condition, Motta et al. [55] perform a detailed collection of flexibility and scale measurement of different shark species that can be valuable for future studies.

Swimming experiment from [57], who used a flat plate covered with real shark skin, also confirm the previous flow control mechanism and also make some conjectures about possible thrust enhancing controlled by the same movable scale that can move away the leading edge vortex.

Also Itoh et al. [41] shows that movable rugosities can outperform riblets, the authors in fact measure the drag reduction of a seal fur (that present fibrous movable surface) against a riblet surface in an experimental channel; its results are show in figure 1.8.

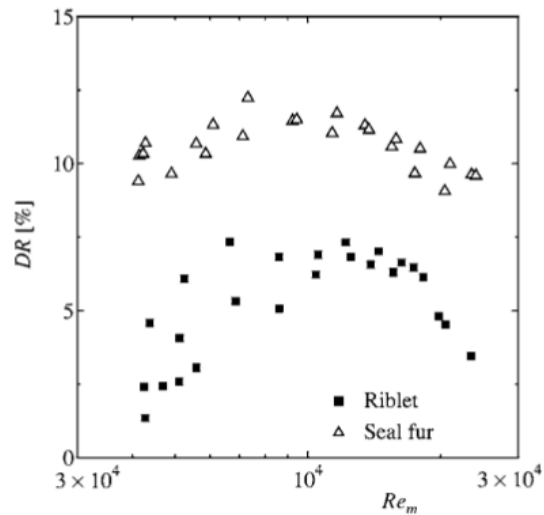


Figure 1.8:  $DR\% = \frac{\Delta\tau}{\tau_0} \%$  Image from Itoh et al. [41].

Compliant surfaces can in fact move accordingly to the surface pressure gradients along the boundary layer and so respond to the pressure fluctuation over the surface itself. This mechanism is already known to be beneficial to delay the transition to turbulence and many authors have presented theoretical and experimental evidence on the effectiveness of this

solution [23], [21].

So we have seen that to reduce turbulent skin-friction drag riblets and natural surfaces uses various mechanism such as: sublayer vortices interaction, compliance and separation control. Such solution have proven to be effective in some cases but they are related mostly in reducing the viscous component of the total drag. In the next section we will introduce another class of solution that try to act instead on the pressure component.

### 1.1.2 Permeable surfaces

Permeable surface has been proposed to exploit even further the mechanism explained above using riblets. There is some experimental evidence that in laminar cases the generation of some *slip velocity*, at the interface between the permeable surface with the fluid, can decrease the friction drag Beavers and Joseph [8]. However in the turbulent case it seems that the instabilities developing at the interface can cause an increase in drag up to 40% Jimenez et al. [43], Breugem et al. [15]; this last mechanism will be further exploited in the section 1.3. Is important to pinpoint that the permeable surface cited in the above references were all rigid.

The resistance pressure contribution is usually the most significant one in bluff bodies applications, and even in highly streamlined body it is around 10% of the total drag. Researchers have tried to find a way to modify the pressure distribution around a bluff body to reduce the associated resistance, and also dump the force oscillation on the body (drag and/or lift).

The pressure drag on a bluff body depends mostly on the difference between the low pressure on the rear part of the body, where there is usually a separated flow region, and the high pressure in the forward part. This idea is sketched in figure 1.9 where two different pressure distribution are shown; the black one represent the classical solid body, and the green one is the one with a porous layer at the back of the body.

The favorable increase in the back pressure is due to the low speed laminar flow in the porous media that is ejected in the back region where the separation take place. Even in very high speed turbulent flow the fluid inside permeable surface exhibit a very high energy loss due to the strong dissipation that the medium provide, resulting so in a low speed flow ejected downstream of the body.

The instability around a cylinder is due to the shear layer that forms in the top part of the body when the flow start to decelerate. This shear layer exhibit a Kelvin–Helmholtz type instability that develop in the classical Von-Karman wake. The permeable interface, producing a slip velocity, can modify the boundary layer that develops above it and with that produce less shear and vorticity.

This two hypothetical mechanisms has been tested numerically by multiple authors: Bruneau and Mortazavi [18], Bruneau and Mortazavi [19], Bhattacharyya and Singh [11], Naito and Fukagata [56]. In their work they have add a porous layer to some classical two dimensional bluff bodies (cylinder, square cylinder, Ahmed body section)and

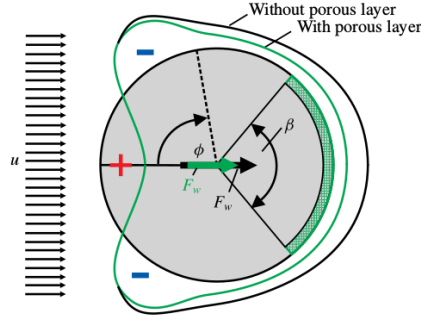


Figure 1.9: Diagram showing an example of pressure distribution around a cylinder for a viscous flow. The black line is the angular distribution as a solid body, the green one is the modified pressure in presence of a porous layer at the rear part. Image from Klausmann and Ruck [44]

performed laminar and turbulent simulation for the flow around such bodies.

These works show some very strong result on multiple quantities, like: decrease of enstrophy, lower root mean square of the lift signal, drag reduction, regularization of the wake and lower pressure gradients; even if the porous medium is always rigid in their case. An example is shown in figure 1.10 where the flow field downstream to a square cylinder is computed in a turbulent case; the picture show how the porous layer strongly regularize the wake.

It seems from the previous works that the medium parameters, like the porous resistance (permeability) or the vertical extension of it, have important effects on the results. They seem to agree (at least qualitatively) that increasing too the porous medium extension over a certain limit is not beneficial, and they also show that the resistance of the medium in order to be effective should not be excessive (medium to high porosity are the best).

In all these work we observe a reduced pressure drop between the front and the rear of the body, a reduced drag, delays in the vortex shedding in the laminar case and regularization on both the frequency and the amplitude of shedded vortices oscillations.

These early work show very optimistic numbers but they should be taken with some care, since only Naito and Fukagata [56] simulations are three-dimensional, and they all use a modeling approach for the porous medium (see section 1.2.2) without any validation of the method, and sometimes they use it outside his field of validity (there is some discussion in the scientific community in using such methods for highly turbulent flows).

Even though the lack of validation reflect the fact that reliable experiment of such porous coatings are almost non existent in literature.

#### DIGRESSION ON THE FORCE BETWEEN A FLUID AND A BLUFF POROUS MEDIUM BODY ? ]

Favier et al. [30] confirms the results on the cylinder using a different numerical method

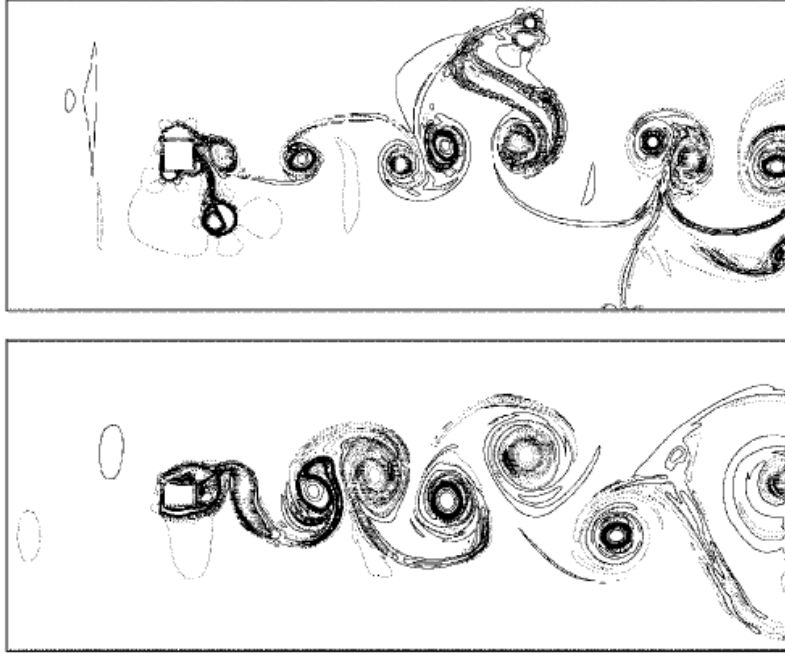


Figure 1.10: Square cylinder vorticity countour for  $Re = 30000$ . Top: solid case. Bottom: porous case with layer extension  $h = 10\%D$ .

The only two experiments find in literature show less promising numbers ...

Heenan and Morrison [39] perform an experiment in which he take a backward facing step with a porous insert in the re-circulation region. His measurement show a 13% decrease of the peak of pressure at the wall and a relocation of the detachment point further downstream. Also depending on the length of the porous insert a maximum of 9% of drag reduction was also observed. The effect of adding a porous surface in this case was to limit the pressure fluctuations that causes the re-circulation bubble unsteadiness.

Later we have some experiment Klausmann and Ruck [44] that show some lower numbers...

Compared to the riblets approach it is clear that a lot has yet to be explained from the physical mechanism involved. The scientific community also need much more experimental data in order to develop new and improved numerical and theoretical models fro such permeable coatings.

However is very difficult to separate the two contribution of the drag (in general, and in this case is impossible due to the porous medium). In all the different versions of the equation for the flow dynamic, velocity and pressure are always coupled, so is not always possible to decouple the different behavior.

## **1.2 Models for flows through porous surfaces**

**1.2.1 Drag that is function of the canopy depth (canopy flow, flow vegetation)**

**1.2.2 Porous media approach through homogenization**

**VANS**

Penalization method Angot et al. [4] used in[18] [19] [20]...

Multiple scales

## **1.3 Stability of flow over permeable surfaces (monami and honami)**

Finnigan [31] Jimenez et al. [43]

**1.3.1 Stability theory generalities**

**1.3.2 Monami Honami**

## Chapter 2

# Volume Average Navier-Stokes Equations

### 2.1 Introduction

### 2.2 Derivation of VANS equations for 3D incompressible fluids

#### 2.2.1 Definition of the averaging filter

In the figure 2.1 is an illustration of our porous problem; in the same figure we show all the main definition that we need to introduce in order to develop our mathematical approach.

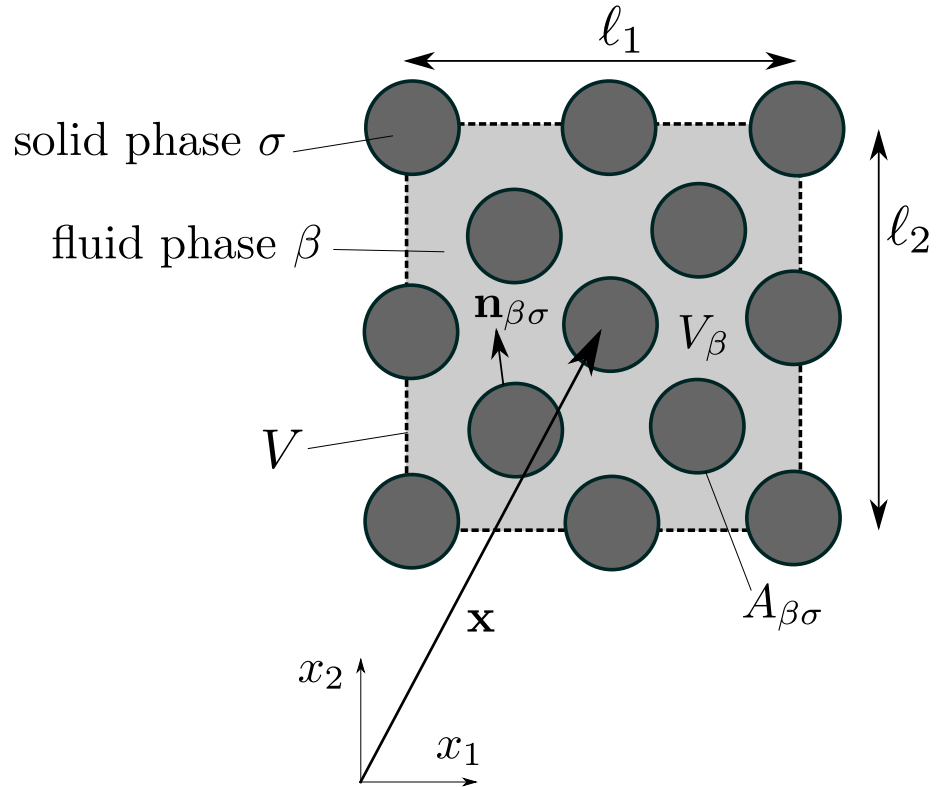


Figure 2.1: Illustration of the REV concept.

$$\langle \psi_\beta \rangle^\beta(\mathbf{X}, t) = \frac{1}{V_\beta} \int_{V_\beta} m(\mathbf{y}) \psi_\beta(\mathbf{x} - \mathbf{y}, t) dV_\beta. \quad (2.1)$$

$$\langle \psi_\beta \rangle^\beta|_{\mathbf{x}} = \frac{1}{V_\beta} \int_{V_\beta(\mathbf{x})} m(\mathbf{y}) \psi_\beta(\mathbf{x} - \mathbf{y}, t) dV_\beta. \quad (2.2)$$

$$\langle \psi_\beta \rangle = \frac{1}{V} \int_{V_\beta} \psi_\beta(\mathbf{x}) dV_\beta. \quad (2.3)$$

$$\varepsilon = \frac{V_\beta}{V} \quad (2.4)$$

$$\langle \psi_\beta \rangle = \varepsilon \langle \psi_\beta \rangle^\beta \quad (2.5)$$

### 2.2.2 Theorems involving derivatives of spatial averaging

**Theorem 2.2.1** (Averaging theorem Howes and Withaker, 1985).

$$\langle \nabla \psi_\beta \rangle = \nabla \langle \psi_\beta \rangle + \frac{1}{V} \int_{A_{\beta\sigma}} \mathbf{n}_{\beta\sigma} \psi_\beta dA$$

### 2.2.3 Length scale decomposition

$$\psi_\beta = \langle \psi_\beta \rangle^\beta + \tilde{\psi}_\beta \quad (2.6)$$

### 2.2.4 Averaged continuity equations

$$\nabla \cdot \mathbf{v}_\beta = 0 \quad (2.7)$$

### 2.2.5 Averaged momentum equations

$$\frac{\partial \mathbf{v}_\beta}{\partial t} + \mathbf{v}_\beta \cdot \nabla \mathbf{v}_\beta = -\frac{1}{\rho_\beta} \nabla p_\beta + \nu_\beta \nabla^2 \mathbf{v}_\beta + \mathbf{f} \quad (2.8)$$

# Chapter 3

## Drag-model sensitivity of Kelvin-Helmholtz waves in canopy flows

### 3.1 Introduction

Flows through submerged aquatic plants exhibit large scale vortices at the top of the vegetation, advecting along the flow direction and causing a periodic waving of the plants, referred to as monami [1]. Vortices arise from the nonlinear amplification of a Kelvin-Helmholtz instability mode, related to the presence of an inflection point in the base flow profile; [5] the profile itself is inflectional because the fluid is slowed down by the drag exerted by the canopy, whose modeling has recently been addressed. [60] [63] [76] The correct prediction of the onset and characteristics of the Kelvin-Helmholtz instability is important for assessing the effects of turbulence, in particular to

- understand how the vertical exchange of momentum occurs, 6
- clarify how the transport of CO<sub>2</sub>, dissolved nutrients or sediments takes place between the obstructed vegetation flow and the free overflow motion, 7–10 and also
- assess the changes in the morphology of the vegetation in inland or coastal wetlands in response to continuous periodic forcing. [5] [58]

Because of the flexibility of the vegetation, some theoretical studies have focussed on the modeling of the stems of the aquatic plants and their displacement in response to the forcing by the water flow. [60] [58] However, Kelvin-Helmholtz vortices occur whether or not the plants bend and—to ascertain causes and effects to first order—it is acceptable to focus on the flow over and through a submerged array of rigid, cylindrical pillars. This has been the basis of the approach by Ghisalberti and Nepf [37] [35] [36] who have conducted a series

of careful experiments; their results have often been used by fluid dynamicists to put forth and test theoretical hypotheses to predict the frequency and wavelength of the large scale vortical motion, for a variety of conditions. The configuration studied consists of a regular grid of rigid pillars, orthogonal to the surface, of identical height  $h$ ; in some of the theoretical models proposed to analyze the stability of this system, the Rayleigh equation is used throughout the water channel, with or without a drag term in correspondence of the canopy. [61] [60] [63] [76] have recently demonstrated that the addition of a drag term through the vegetation reduces the amplification factor of the Kelvin-Helmholtz instability throughout the whole range of wavenumbers and increases mildly the wavelength of the fastest growing mode; further unpublished work by the same authors shows that the addition of a mixing length turbulence model in the stability equations has but a negligible influence on the leading instability mode. Questions remain, however, on the accuracy of the drag model and on its sensitivity. A partial answer to these questions is provided in [76]: there, a different model, applicable within the vegetated layer and based on the equations ruling the behavior of a transversely isotropic porous medium, has been developed and the stability results appear to better match experimental correlations. This conclusion is, however, not consolidated yet, and further studies are needed to assess the influence of the model of the drag force through the vegetation, both in setting up a particular (inflectional) mean flow and on the onset and growth of Kelvin-Helmholtz waves. The present work addresses the points above through an adjoint-based sensitivity analysis along the lines of [14] the direct stability equations are written with account of viscosity, and the adjoint equations are found and solved in the temporal framework. Results in the spatial setting are discussed in Appendix B, where a digression is made on the computation of the group velocity of the instability waves by the use of the adjoint fields. The sensitivity functions to both mild modifications in the base shear layer and in the drag coefficient are computed and discussed. Finally, a different sensitivity analysis is developed on the basis of the recent anisotropic model by [76] and the results qualitatively compared to those obtained with the more conventional isotropic-drag-force model.

## 3.2 Model of the canopy flow

### 3.2.1 The mean flow

To obtain the mean flow on top of which small amplitude perturbations are superimposed, the procedure outlined by [35] and recently closely followed by [76] is used. For the sake of conciseness, the procedure which relies on several empirical correlations is not repeated here, aside from a few brief comments. A mildly inclined water channel is considered, with a canopy formed by rigid cylindrical dowels of height  $h$  equal to  $13.8\text{ cm}$  and diameter  $d = 0.64\text{ cm}$ . The frontal area of the vegetation per unit volume, i.e., the packing density of the elements, is either  $a = 0.04\text{ cm}^{-1}$  or  $0.08\text{ cm}^{-1}$ ; the free surface is positioned at a level  $H = 46.7\text{ cm}$  from the bottom plate and the flow velocity at the free surface,  $U_2$ , varies

from 4.4 to  $13.7\text{cm/s}$ . The Froude number,  $F_r = \frac{U_2}{gH}$  is thus very low and water surface fluctuations can be ignored [16]. To a good approximation the mean flow can be taken as steady and parallel, with the streamwise velocity varying from the value  $U_1$  at the bottom wall (not accounting for the thin bottom boundary layer) to the value  $U_2$  at the top, near the free surface (3.1). The slope of the bottom surface is very small; it is denoted as  $S$  and, in the experiments by [35] varies from  $1.8 \times 10^{-6}$

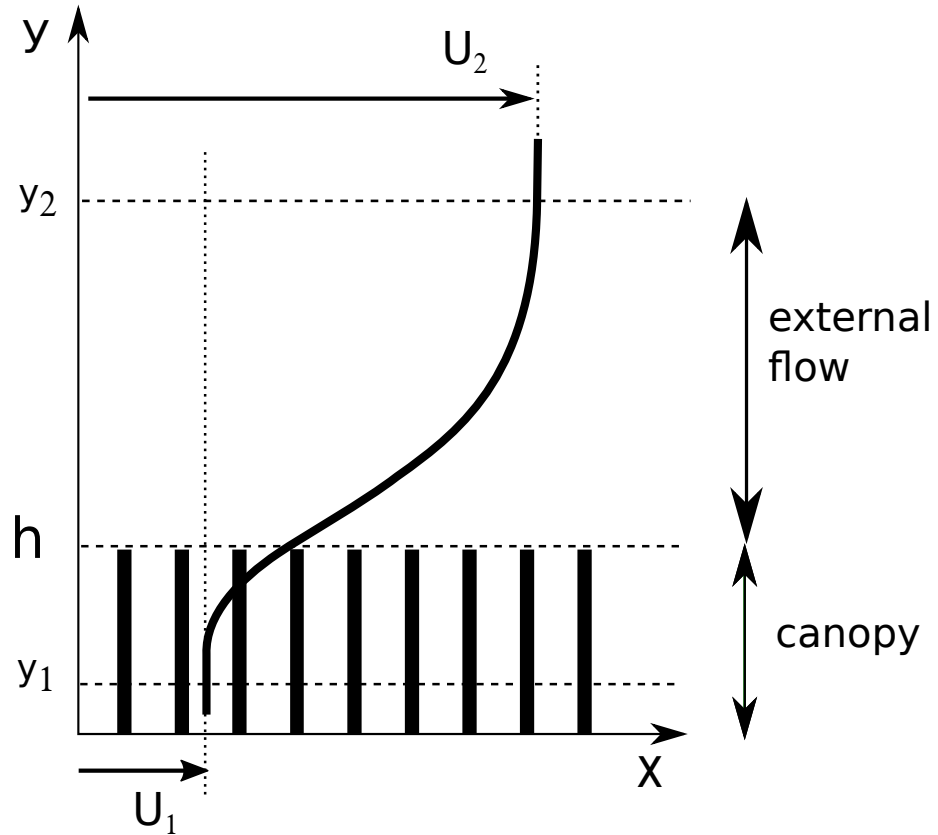


Figure 3.1: Configuration studied with main notations

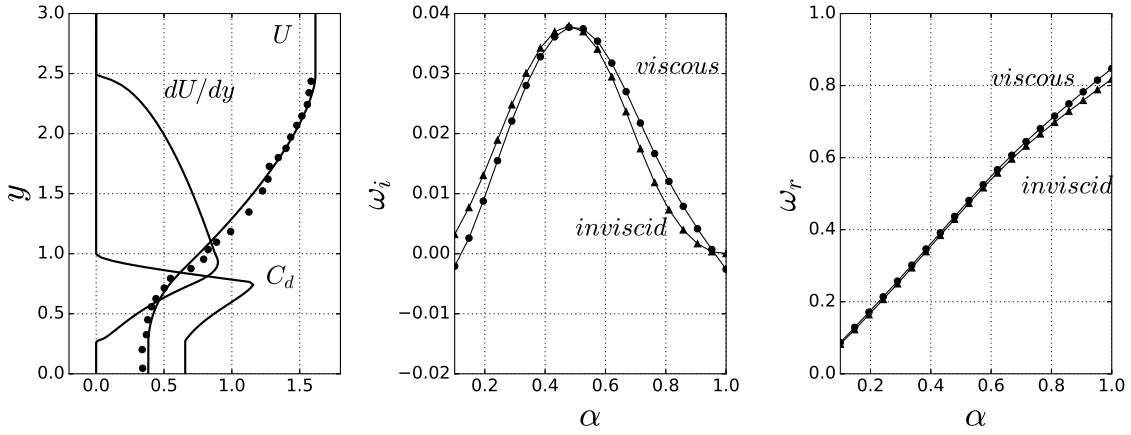


Figure 3.2: Left frame: mean flow  $U$ , together with experimental data points [35], its first derivative, and drag coefficient distribution (case G). Center: viscous and inviscid growth rates,  $\omega_i$ , as a function of the streamwise wavenumber  $\alpha$ . Right: corresponding frequencies,  $\omega_r$

to  $10^{-4}$ ; such a slope provides the driving force for the motion. The viscous term is small compared to the turbulent diffusion term, so that the mean streamwise momentum equation can be approximated by

$$gS = \frac{\partial \bar{u}' \bar{v}'}{\partial y} + \frac{1}{2} C_D(y) a U(y)^2 \quad (3.1)$$

with  $g$  the acceleration of gravity and  $C_d$  an isotropic drag function available from the experiments, variable across the canopy and equal to zero when  $y \geq h$ . The Reynolds stress  $\bar{u}' \bar{v}'$  is modelled with the Boussinesq assumption, introducing a turbulent viscosity which depends on a mixing length and on the gradient of the mean velocity  $U$ . Referring to [35] for details of the empirical correlations used to close the equations and the solution method, we limit ourselves here to stating that the results obtained for the mean flow are very close to those reported in [76] (cf. their Figure 3) and closely match experimental points for the cases G, H, I, and J considered (we use the same terminology of [37] [35] [36] to indicate the different flow configurations). An example of mean flow is reported in 3.2 (left frame). There, one can observe the computed flow (against discrete measurement points), its first derivative, and the drag coefficient distribution for one representative case (experiment G), used below also to discuss stability and sensitivity results. Other procedures have been employed in the past to calculate the mean flow, with satisfactory results. For example, [63] have considered a constant value of  $C_d$  through the canopy, while [76] have coupled, at a fictitious interface, the fluid equations outside the canopy to Darcy's law within the vegetation. Thus, for the purposes of the present paper, the mean flow is assumed as given; it could be, for example, simply a fit through experimental data.

Nonetheless, in Appendix A we provide some considerations on how  $C_d$  affects the mean flow in the model used here.

### 3.2.2 Stability and sensitivity equations

A temporal linear stability analysis is carried out, with the generic perturbation  $q'(x, y, t)$  of the form

$$q'(x, y, y, t) = \tilde{q}(y)e^{i(\alpha x - \omega t)} \quad (3.2)$$

with  $\alpha$  the real streamwise wavenumber and  $\omega$  a complex number whose real part,  $\omega_r$ , is the frequency of the mode and the imaginary part,  $\omega_i$ , is the growth rate. The dimensionless linear stability equations in primitive variables read

$$\begin{aligned} i\alpha u + Dv &= 0, & D &= d/dy \\ \left[ i(\alpha U - \omega) - \frac{D^2 - \alpha^2}{Re} + aC_d U \right] u + U' v + i\alpha p &= 0, & U' &= \frac{dU}{dy} \\ \left[ i(\alpha U - \omega) - \frac{D^2 - \alpha^2}{Re} \right] v + Dp &= 0 \end{aligned} \quad (3.3)$$

with the perturbation velocity components which vanish when  $y = 0$  and  $y_\infty$ . The upper boundary of the computational domain is taken far enough away from the lower boundary to ensure that the results do not vary upon modifications of  $y_\infty$ . All the terms in the equations are dimensionless; the mean speed through the shear layer,  $U_m = \frac{U_1 + U_2}{2}$ , is used to scale the disturbance velocity components, pressure is scaled with  $\rho U_m^2$ , distances with  $h$ , and time with  $h/U_m$ . The Reynolds number in the equations above is thus defined as  $Re = \rho U_m / \mu h$ , with  $\rho$  and  $\mu$  the fluid's density and dynamic viscosity, respectively. The computations are performed both at the  $Re$  values of the experiments and in the inviscid limit ( $Re^{-1} \rightarrow 0$ ), for comparison purposes. In the latter case, the boundary conditions are simply  $v = 0$  at  $y = 0$  and  $y_\infty$ . System 3.3 above and its boundary conditions are, in the following, also written in short notation as  $\mathcal{L}q = 0$ . The eigenvalues of the system are those complex values of  $\omega$  which yield non-trivial solutions for  $u$ ,  $v$ , and  $p$ . Two numerical collocation codes are written, and successfully compared; one is based on the equations in primitive variables form, the second solves an Orr-Sommerfeld-like equation (with the addition of the drag term) along the lines of [63]. In both cases, a spectral scheme based on N Chebyshev polynomials is used (N is typically equal to 300 to ensure grid-converged results), with an algebraic mapping between the physical and the spectral domains ([40]). Viscous and inviscid stability results for case G are shown in 3.2 (center and right frames); differences are small, in consideration of the fact that the Reynolds number of the viscous case is relatively large ( $Re = 3450$ ). The viscous wavenumber of largest amplification is

found for  $\alpha = 0.4790$ ; the waves are weakly dispersive, particularly at low wavenumbers (an original interpretation of phase and group velocities is proposed in Appendix B). The wavelength of largest growth is smaller than that found by [76] which was 0.73; this is related to the slightly different base flow in the two cases (in the present contribution a smoothing has been applied to the  $U$  velocity distribution to render  $dU/dy$  continuous across  $y$ ) and highlights the sensitivity of this stability problem to base flow variations. Following [14] it is assumed that small variations in base flow and drag coefficient entail infinitesimal variations in the system's eigenvalues and eigenfunctions. We stress here the fact that  $C_d$  is identically equal to zero outside of the canopy, and this implies that there are no possible variations in  $C_d$  for  $y \geq 1$ . The sensitivity functions to variations in  $U$  and  $C_d$  are obtained by using the properties of the adjoint system which is defined from the Lagrange identity

$$0 = \delta\langle q^\dagger, \mathcal{L}q \rangle = \langle q^\dagger, \mathcal{L}\delta q \rangle + \langle q^\dagger, \frac{\partial \mathcal{L}}{\partial U} q \delta U \rangle + \langle q^\dagger, \frac{\partial \mathcal{L}}{\partial C_d} q \delta C_d \rangle + \langle q^\dagger, \frac{\partial \mathcal{L}}{\partial \omega} q \rangle \delta \omega \quad (3.4)$$

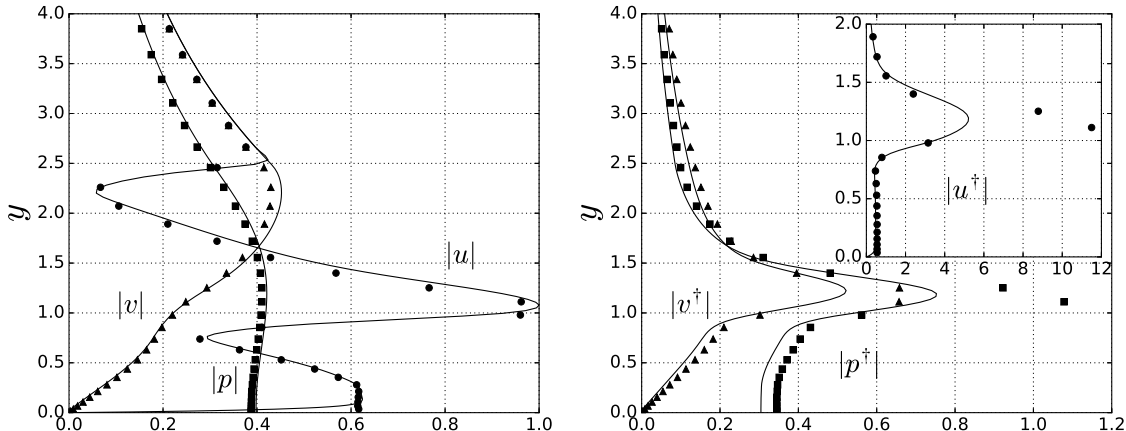


Figure 3.3: Moduli of direct (left frame) and adjoint (right frame) eigenfunctions for the viscous (continuous lines,  $Re = 3450$ ) and the inviscid (symbols) case, in correspondence to the wavenumber of largest amplification.

and considering the effect of independent variations of  $U$  and  $C_d$  onto  $q$  and  $\omega$ . It is found that

$$\delta\omega = \delta\omega_r + i\delta\omega_i = \int_0^{y_\infty} G_U(y)\delta U(y)dy + \int_0^1 G_{C_D}(y)\delta C_D(y)dy \quad (3.5)$$

with

$$\begin{aligned} G_U &= \alpha \left[ \bar{v^\dagger v} + \bar{u^\dagger u} \right] + i(\bar{u^\dagger v})' - iaC_d \bar{u^\dagger u} \\ G_{C_d} &= -iaU \bar{u^\dagger u} \end{aligned} \quad (3.6)$$

the required sensitivity functions; the real parts of  $G_U$  and  $G_{C_d}$  express sensitivities to variations in the frequency of the mode while the imaginary parts are sensitivities to variations in the growth rate. Direct and adjoint eigenfunctions are normalized so that  $N_\omega = 1$ , with

$$N_\omega = \int_0^{y_\infty} \left[ \bar{v^\dagger v} + \bar{u^\dagger u} \right] dy \quad (3.7)$$

An example of direct and adjoint eigenfunctions is provided in 3.3, both in the viscous case ( $Re = 3450$ ) and in the inviscid limit, for  $\alpha = 0.4790$ . It is interesting to observe that while the direct eigenfunctions are almost overlapped, the same is not the case for the adjoint eigenfunctions, with the inviscid mode (drawn with symbols) which has a larger amplitude than the viscous one. The shapes of the direct eigenfunctions are very close to those reported in [76]. The adjoint modes reveal that the flow is most sensitive to streamwise forcing, particularly when it occurs slightly above the edge of the canopy. Source terms in the mass conservation and in the vertical momentum equations are much less effective.

### 3.3 SENSITIVITY RESULTS FOR THE ISOTROPIC DRAG MODEL

Some representative sensitivity functions are plotted in 3.4; viscous and inviscid results concur in showing that the largest sensitivities to variations of  $U$  are found right above the vegetation's edge, where there are peaks in the adjoint eigenfunctions and where  $d^2U/dy^2$  vanishes. The  $U$ -sensitivities are negligible within the vegetated layer and for values of  $y$  larger than twice the canopy's height. The  $C_d$ -sensitivities are non-negligible only in close proximity of the interface. It is interesting to observe that real and imaginary parts of the  $U$ -sensitivity functions are shifted in  $y$  with respect to one another; this means that, for example, a localized perturbation at a given  $y$  position (above the canopy) might have a strong repercussion on the growth rate but not on the frequency of the most unstable Kelvin-Helmholtz mode, or vice versa. Comparing left and right frames of the figure, it is seen that inviscid  $G_U$  sensitivity functions display sharper peaks and steeper gradients, and yield larger variations in  $\omega$  than their viscous counterparts in the proximity of the  $U$  inflection point, a clear consequence of the inviscid mechanism ruling the instability. In both the viscous and the inviscid models, the sensitivity to base flow variations is typically one order of magnitude larger than the sensitivity to changes in the drag coefficient.

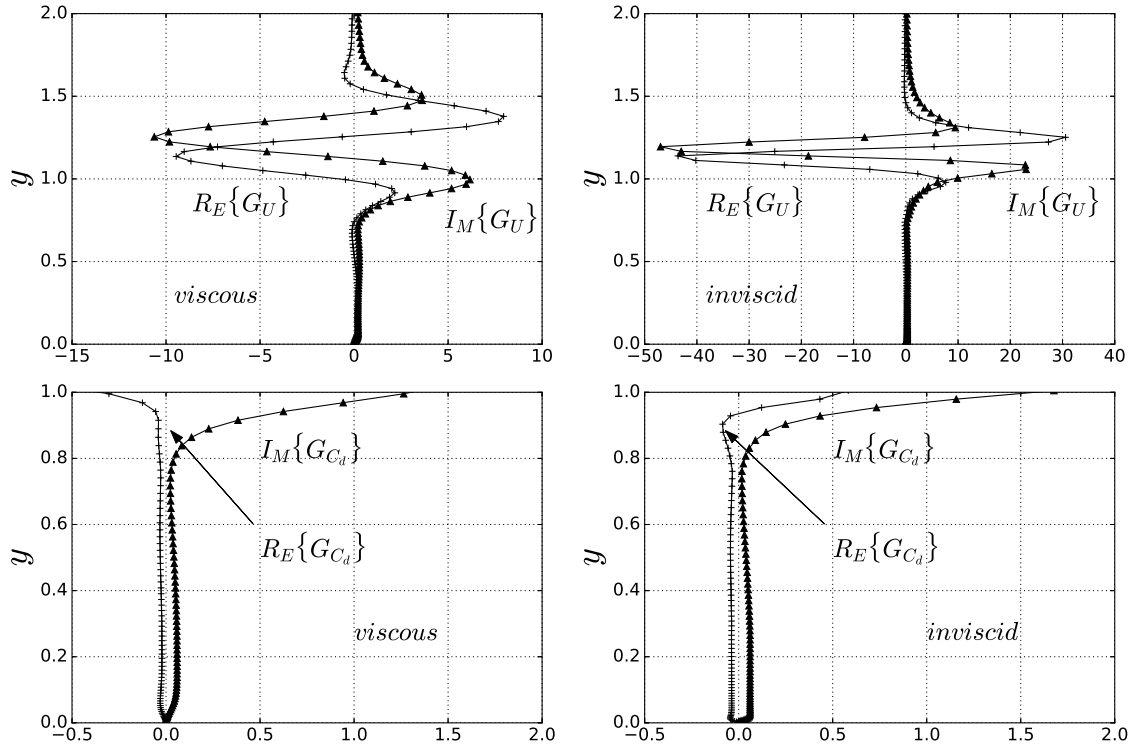


Figure 3.4: Real and imaginary parts of the sensitivities to mean flow variations (top) and to variations in the drag distribution function (bottom), for the parameters of 3.3

The infinite norm of the sensitivities for the four cases studied (G, H, I, and J) is reported in 3.5; the main result found is that  $|G_U|_\infty$  grows monotonically with  $\alpha$  (and more so in the inviscid case) whereas  $|G_{C_d}|_\infty$  does not. It is consistently found that  $|G_U|_\infty$  of case H is larger than that of case I, which exceeds the corresponding value of case J, in turn larger than  $|G_U|_\infty$  of case G. This is not unexpected in view of the values of the mean shear  $\frac{U_2 - U_1}{H}$  which are, going from H to G, equal

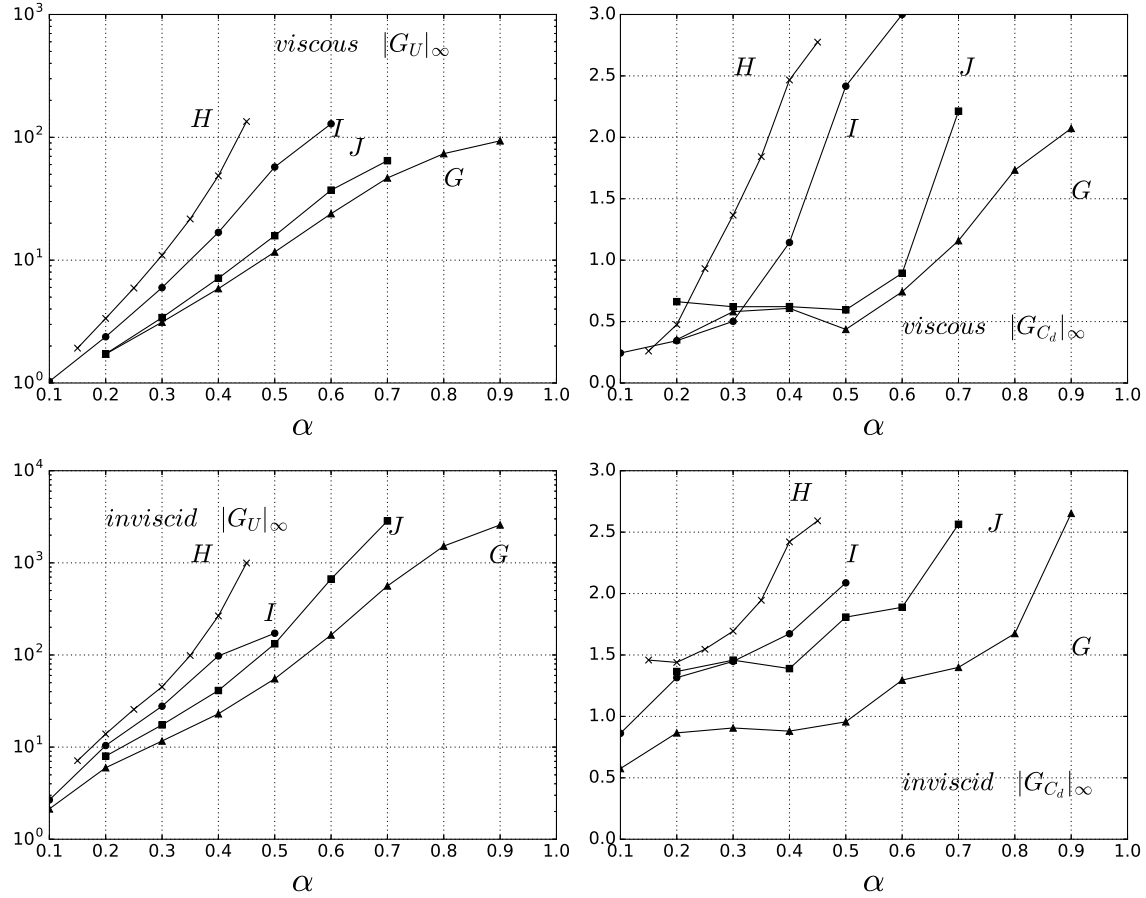


Figure 3.5: Infinite norms of the sensitivity functions for varying  $\alpha$

to  $0.236$ ,  $0.158$ ,  $0.084$ , and  $0.071 s^{-1}$ , respectively. The sensitivity of the eigenvalue  $\omega$  to variations in the mean flow is generally stronger than the corresponding sensitivity to variations in the drag coefficient (aside for the long wave limit, where they are comparable). This might be interpreted positively, considering that the use of a scalar coefficient  $C_d$  to represent the drag within the canopy is but a crude approximation. An alternative model to represent the flow throughout a network of rigid, cylindrical dowels has recently been proposed by [76]. The sensitivity results for such a new model are discussed next.

### 3.4 AN ALTERNATIVE SENSITIVITY MODEL: ACCOUNTING FOR THE CANOPY ANISOTROPICITY

The stability problem in this section is based on the coupling between two regions, one outer region dominated by inertia and ruled by the inviscid equations and an inner one dominated by viscosity and ruled by Darcy's law, with account of the canopy geometry through a tensorial permeability, as described by [76] Normalizing the disturbance equation which couples pressure and velocity in the inner region with the same scales as previously, we obtain

$$u_i' = -Re \frac{d}{ah^2} \mathcal{K}_{ij} \frac{\partial p'}{\partial x_j}, \quad (x_1, x_2) = (x, y) \quad (3.8)$$

with  $\mathcal{K}_{ij}$  the dimensionless permeability. The effective interface between the inertial region and the slow, viscosity-dominated region does not coincide with the edge of the canopy; in fact, the rapid outer flow penetrates through the upper part of the vegetation and an effective matching between outer and inner flows must be enforced some distance  $\delta$  below the canopy's edge [49]. This distance, a penetration depth, has been successfully computed by [73] for a few cases and is found to increase with the Reynolds number of the flow; for experiment G discussed below it is  $\delta = 0.40$  [74]. On account of the results shown in 3.4, with the sensitivities which are negligible for  $y \approx 0.60$ , we expect that the exact position of the effective interface will not affect the results significantly. Using the fact that the velocity within the orthotropic porous medium is divergence free, the interface condition to be applied at  $y_{itf} = 1 - \delta$  is found to be 3.9

$$v|_{itf} + B(\alpha)p|_{itf} = 0 \quad (3.9)$$

with

$$B(\alpha) = Re \frac{d}{ah^2} \sqrt{\mathcal{K}_{11} \mathcal{K}_{22}} \alpha \tanh(\theta), \quad \theta = \alpha \sqrt{\frac{\mathcal{K}_{11}}{\mathcal{K}_{22}}} y_{itf}$$

The second boundary condition that the Rayleigh stability equation must satisfy at  $y_\infty$  is simply  $v = 0$ . Thus, we solve only for the inviscid flow in the outer region, and the permeability of the inner domain enters the equations only through the interface condition 3.9.  $\mathcal{K}_{ij}$  is a two- by-two diagonal tensor;  $\mathcal{K}_{11}$  is the component of the dimensionless permeability along  $x$  and  $\mathcal{K}_{22}$  is the  $y$  component. For case G considered here, the packing density of the elements is  $a = 0.04\text{cm}^{-1}$ ; it is also found that  $\mathcal{K}_{11} = 0.0512$  and  $\mathcal{K}_{22} = 0.0575$  [74], so that the function  $B(\alpha)$  reads  $B = 15.727\alpha \tanh(0.566\alpha)$ .

### 3.4.1 The sensitivity equations

The adjoint equations in this case are the same as system 3.3, without the terms containing  $1/Re$  and  $C_d$ , and the boundary conditions are

$$v^\dagger|_{itf} - B(\alpha)p^\dagger|_{itf} = 0, \quad v^\dagger|_{y_\infty} = 0 \quad (3.10)$$

The variation in the complex frequency is related to variations in the mean flow and in the permeability components through the equation

$$\delta\omega = \int_{y_{itf}}^{y_\infty} G_U(y)\delta U(y)dy + G_{\mathcal{K}_{11}}\delta\mathcal{K}_{11} + G_{\mathcal{K}_{22}}\delta\mathcal{K}_{22}$$

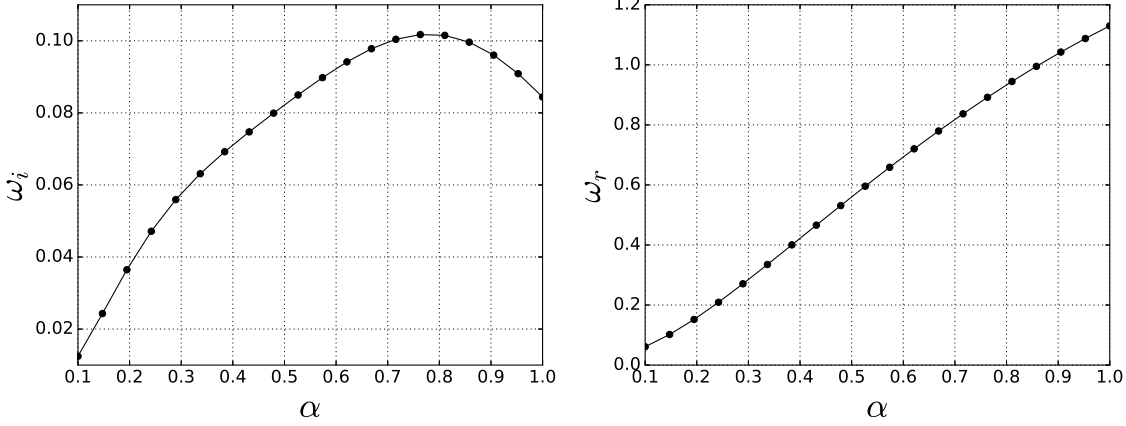


Figure 3.6: Amplification factor (left) and frequency of the most unstable mode as a function of  $\alpha$ , for the anisotropic drag model

with

$$\begin{aligned} G_U &= \alpha \left[ \overline{v^\dagger v} + \overline{u^\dagger u} \right] + i(\overline{u^\dagger v})' \\ G_{\mathcal{K}_{11}} &= -\frac{i}{2}\alpha Re \frac{d}{ah^2} \left[ \overline{p^\dagger p} \right] |_{itf} \sqrt{\frac{\mathcal{K}_{22}}{\mathcal{K}_{11}}} \left\{ \tanh \theta + \frac{\theta}{\cosh^2 \theta} \right\} \\ G_{\mathcal{K}_{22}} &= -\frac{i}{2}\alpha Re \frac{d}{ah^2} \left[ \overline{p^\dagger p} \right] |_{itf} \sqrt{\frac{\mathcal{K}_{11}}{\mathcal{K}_{22}}} \left\{ \tanh \theta - \frac{\theta}{\cosh^2 \theta} \right\} \end{aligned} \quad (3.11)$$

the required sensitivities, with the normalization  $\int_{y_{itf}}^{y_\infty} [\overline{v^\dagger v} + \overline{u^\dagger u}] = 1$ . In writing  $\delta\omega$  above, we have made the assumption that the mean flow  $U$  does not vary at the two extreme points of the integration domain. The stability results (for the same parameters as in 3.2)

are displayed in 3.6. As already observed in [76], both the growth rate and the frequency are slightly larger with this model than with the isotropic resistance model, for all  $\alpha$ 's, and the most unstable mode is found at a larger value of  $\alpha$  (here  $\alpha \approx 0.8$ ) in better agreement with experimental correlations [76] [61]. Also in this case the waves are found to be only weakly dispersive. Eigenfunctions are plotted in 3.7, together with the real and imaginary parts of the  $G_U$  sensitivity function. As in 3.3, the modulus of the  $u$  eigenfunction peaks near the edge of the canopy ( $y = 1$ ), whereas the adjoint eigenfunctions have a maximum value slightly above. As a general remark, the shapes of the direct and adjoint modes are quite similar to those found with the isotropic resistance model; as reported at the end of 3.2.2, it is found that the flow is most sensitive to streamwise momentum forcing. Also, real and imaginary parts of  $G_U$  have a double-peak structure, like in the isotropic-drag model, but now the largest absolute value of  $G_U$  is

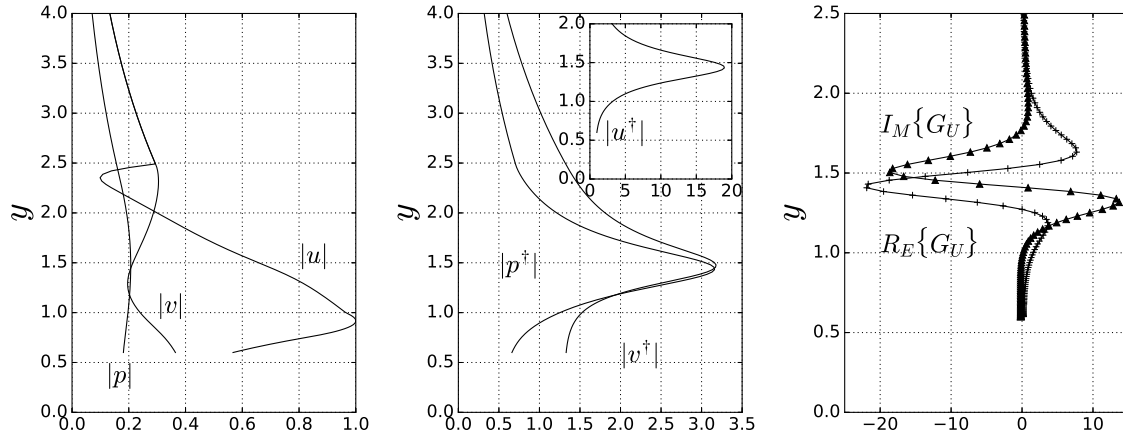


Figure 3.7: Left and center frames: moduli of direct and adjoint eigenfunctions; pressure and “adjoint pressure” are drawn with dashed lines. Right: real and imaginary parts of the sensitivity function  $G_U$  ( $\alpha = 0.4790$ )

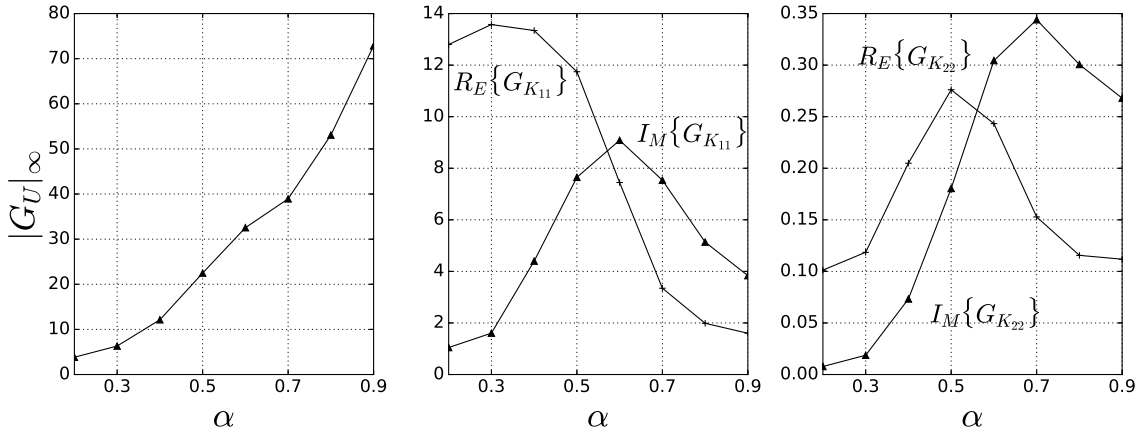


Figure 3.8: Case G. Left: infinite norm of  $GU$  for varying  $\alpha$ . Center and right frames: real and imaginary parts of the sensitivity coefficients to variations in the permeability components

smaller and shifted towards a larger  $y$  than in the previous inviscid case (cf.3.4, top-right frame). This can also be appreciated by the inspection of 3.8 (left);  $|GU|_\infty$  still grows monotonically with  $\alpha$ , but the sensitivity is smaller than that computed earlier (cf. 3.5) with either the viscous or inviscid model (it is actually closer to the viscous sensitivity, as an effect of the interface condition). Furthermore, it is interesting to observe that both real and imaginary parts of  $GU$  vanish for  $y = y|_{itf}$  (cf.3.7, right), and this supports the statement made previously that a small shift in the position of the effective interface has but a minor influence on the most unstable mode. The sensitivity coefficients for the two components of the permeability tensors are displayed in 3.8 (center and right frames): the present model is more effective to variations in  $K_{11}$  than to  $K_{22}$  as far as modifying the complex eigenfrequency. Significantly, different ranges of wavenumbers behave differently as far as the variation in  $\omega$  is concerned. The frequency  $\omega_r$  of long waves (around  $\alpha \approx 0.3$ ) is more easily modified by acting on  $K_{11}$  (with an almost negligible effect on the growth rate of the wave); conversely, the growth rate of modes with large values of  $\alpha$  is affected efficiently by variations in the first component of the permeability tensor.

### 3.5 CONCLUDING REMARKS

We have considered two different models of the flow through a vegetated layer experiencing Kelvin-Helmholtz destabilization. One model is based on the use of a single drag coefficient to express the force exerted by the vegetation on the fluid, the second considers the canopy as an orthotropic porous medium and is based on Darcy's equation with a tensorial permeability [73]. Both models have advantages and drawbacks. The main

advantage of the first model is that the drag coefficient can be taken to vary across the canopy; whether this positive consideration, based on macroscopic experimental measurements [37] [35] [36], carries over to the stability problem remains to be established. The second model, applicable to dense porous media, considers two independent parameters to express the disturbance flow perpendicular and parallel to the rigid dowels forming the canopy. Such parameters and components of the transversely isotropic permeability tensor  $K_{ij}$  arise from the solution of a local Oseen problem [73]. The drawback of the second model is the fact that an interface (whether real or effective) appears, and adequate matching conditions must be enforced there. Despite much work since the seminal contribution by [7], a consensus on the “best” interface conditions between a pure fluid region and a porous medium has not yet emerged. The models have been put to test through a classical sensitivity analysis [14]. Beyond displaying stability results which correspond better to those to be expected from available experimental correlations [61] [76], the anisotropic model is less sensitive to variations in the base flow (with potentially larger variations in frequency and growth rate of the instability mode for the case of shorter waves). As far as a direct comparison between  $G_{C_d}$  and  $G_{K_{ii}}$  is concerned, this can hardly be made since the variables represent different objects; in particular, the pressure drop through the canopy depends directly on  $C_d$  and inversely on the permeability. The present results indicate that the anisotropic model depends significantly on the value of the apparent [73] permeability component  $K_{11}$ , whose evaluation must thus be conducted carefully. This model is also of interest for further developments, in particular for the study of instabilities developing over waving canopies. Darcy’s law in this latter case would need to be modified, as described in [54] and [75].

## Acknowledgment

The authors would like to thank the IDEX Foundation of the University of Toulouse for the financial support granted to the last author under the project “Attractivity Chairs.” The computations have been conducted at the CALMIP center, Grant No. P1540. The referees are gratefully acknowledged for their comments leading, in particular, to the correct interpretation of the sensitivity of the drag coefficient and to the material in Appendix A.

## APPENDIX A: EFFECT OF $C_d$ ON THE MEAN FLOW

In 3.2 of the paper it is described how the eigenvalue  $\omega$  varies as an effect of independent variations of  $U$  and  $C_d$ . However, since  $C_d$  is not zero within the canopy and it is used to compute the mean flow profile  $U$ , we should in principle have expressed  $\delta U$  as  $\delta U = \frac{dU}{dC_d} \delta C_d$  and considered a single sensitivity function  $G^*_{C_d} = G_{C_d} + \frac{dU}{dC_d} G_U$ , instead of the two sensitivities given in 3.6. This would have certainly been the appropriate line

of action if the mean flow equation were issued from exact equations, in which case we should have considered also the adjoint of the base flow equation in our variational problem. However, the mean flow model by [35] contains empirical approximations and parameters, and alternative models [63], [76]—including very different ones—have been used successfully in the past to predict the mean field; we have thus made the choice, in both 3.3 and 3.4, of considering the mean flow as given, and to take independent variations of  $U$  and  $C_d$  in the stability analysis to assess the effect of modifications in either variable. If we were to find how much the base flow depends on the drag coefficient in this particular problem, we would need to determine the function  $U(C_d)$  and take its derivative. Since both  $U$  and  $C_d$  are functions of the space coordinate  $y$ , the implicit dependence can be found, and we have plotted it for one case on the left frame of 3.9. Clearly, the function  $U = f(C_d)$  is not single-valued and therefore the derivative can be calculated only over two separate  $U$  (or, equivalently,  $y$ ) intervals. We have carried out the derivation numerically over each interval, within the range  $0.3 \leq y \leq 1$ , and the result is reported on the right frame of 3.9. The filled triangle and circle symbols indicate the two  $y$  intervals within the canopy. We first observe that both the location where  $C_d$  is maximum and the shape of the function  $U = f(C_d)$  are strongly correlated to the drag law  $C_d(y)$ , modeled by [35]

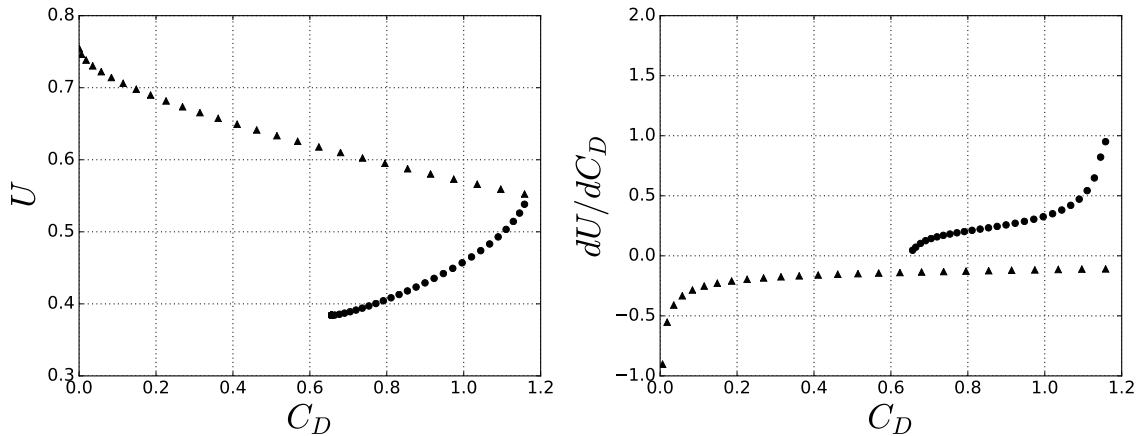


Figure 3.9: Case G. Left: mean velocity profile,  $U$ , versus the drag coefficient,  $C_d$ . Right: first derivative,  $dU/dC_d$ . The triangles denote the region  $y \in [0.76, 1]$ , the filled circles denote the region  $y \in [0.3, 0.76]$ .

through their measurement data (cf. their Figure 7 and Equation (18)). We also notice that the derivative  $dU/dC_d$  is reasonably small except locally at the point where the derivative of the function is not continuous, where it is of order 1. The discontinuity there is however artificial since the function  $C_d(y)$  given in Equation (18) of [35], where  $C_d$  is divided into a parabolic and a linear part, can be easily modified to yield a continuous first derivative at  $y = 0.76$  if required, still maintaining a mean flow very close to the measured

one.

## APPENDIX B: A DIGRESSION ON SPATIAL STABILITY THEORY AND GROUP VELOCITY

Stability problems such as the first one considered in this paper can be approached with the spatial theory framework, with the wavenumber  $\alpha$  complex, its imaginary part being a growth rate, and the circular frequency  $\omega$  a real constant parameter. Let us generalize the sensitivity analysis by considering, as a first step,  $\alpha$  and  $\omega$  as complex numbers which can vary. Equation 3.4 contains one additional term and reads:

$$0 = \delta\langle q^\dagger, \mathcal{L}q \rangle = \langle q^\dagger, \mathcal{L}\delta q \rangle + \langle q^\dagger, \frac{\partial \mathcal{L}}{\partial U} q\delta U \rangle + \langle q^\dagger, \frac{\partial \mathcal{L}}{\partial C_d} q\delta C_d \rangle + \langle q^\dagger, \frac{\partial \mathcal{L}}{\partial \omega} q \rangle \delta \omega + \langle q^\dagger, \frac{\partial \mathcal{L}}{\partial \alpha} q \rangle \delta \alpha \quad (3.12)$$

To obtain the sensitivities in the spatial problem (for which  $\delta\omega = 0$ ) we now have to solve an adjoint system similar to 3.3, where  $\omega^\dagger$  is replaced by  $\omega$  and  $\alpha$  by  $\alpha^\dagger$ . The variation of the wavenumber  $\delta\alpha = 0$  is thus given by:

$$\delta\alpha = \delta\alpha_r + i\delta\alpha_i = \int_0^{y_\infty} G_U(y)\delta U(y)dy + \int_0^1 G_{C_d}(y)\delta C_d(y)dy$$

the functions  $G_U$  and  $G_{C_d}$  maintain the same form as in the temporal theory 3.6, with the direct and adjoint eigenfunctions which are now normalized by imposing that  $N_\alpha = -1$ , with

$$N_\alpha = \int_0^{y_\infty} \left[ \left( U - \frac{2i\alpha}{Re} \right) (\bar{v}^\dagger v + \bar{u}^\dagger u) + \bar{p}^\dagger u + \bar{u}^\dagger p \right] d y$$

Let us now consider a problem in which  $U$  and  $C_d$  are not allowed to vary, but  $\alpha$  and  $\omega$  are. With reference to Equation 3.12, with any choice of normalization of direct and adjoint modes, it is found that  $N_\omega\delta\omega = N_\alpha\delta\alpha$ . Thus, once the adjoint problem is solved, it is possible to accurately compute the group velocity  $c_g$  of any stability problem using the value of  $N_\omega$  and  $N_\alpha$ , i.e.,

$$c_g := \frac{d\omega_r}{d\alpha_r} \approx \frac{\text{real}(N_\alpha)}{\text{real}(N_\omega)} \quad (3.13)$$

Note that  $c_g$  above is different from the “complex group velocity”  $C_g := \frac{d\omega}{d\alpha} \approx \frac{N_\alpha}{N_\omega}$ , and it is also  $c_g \neq \text{real}(C_g)$ . Relation 3.13 can be employed in either a spatial or temporal stability analysis and some representative results (for case G) are provided in Table I with the phase velocity  $c_r := \omega_r/\alpha_r$  and the group velocity determined from Equation 3.13. The temporal or spatial amplification factors,  $\omega_i$  or  $-\alpha_i$ , respectively, are also given for all

cases using Gaster's transformation:  $\omega_i = -\alpha_i c_g$ . Two types of errors on the calculation of the group velocity (noted  $err$ ) are given in the table; the top four values, relative to the temporal theory, are defined as

$$err = \frac{|c_g|_{3.13} - c_g|_{FD}|}{c_g|_{3.13}}$$

with  $c_g|_{FD}$  arising from a first-order finite difference approximation of the group velocity. The bottom four values are defined by the formula

$$err = \frac{|c_g|_{temporal} - c_g|_{spatial}|}{c_g|_{temporal}}$$

The relative difference on  $c_g$  between temporal and spatial theory is rather low. It has to be kept in mind, however, that a stability analysis in the spatial framework yields a nonlinear eigenvalue problem, with a consequent larger numerical system than in the temporal framework; therefore, by inverting matrices of the same size, the accuracy is expected to be slightly lower. The accuracy of the growth rate approximated through Gaster's relationship is also found to be acceptable.

Theory	$Re$	$\alpha_r$	$\omega_r$	$-\alpha_i$	$\omega_i$	$c_r$	$c_g$	$err(\%)$
Temporal	500	<b>0.5</b>	0.4778	<i>0.0248</i>	0.0254	0.9556	1.0245	0.54
	3450	<b>0.5</b>	0.4601	<i>0.0413</i>	0.0404	0.9202	0.9797	0.06
	$10^5$	<b>0.5</b>	0.4514	<i>0.0436</i>	0.0421	0.9028	0.9661	0.63
	$10^9$	<b>0.5</b>	0.4508	<i>0.0451</i>	0.0425	0.9016	0.9427	2.90
Spatial	500	0.4993	<b>0.4778</b>	0.0248	0.0250	0.9569	1.0100	1.41
	3450	0.4990	<b>0.4601</b>	0.0427	0.0404	0.9220	0.9471	3.30
	$10^5$	0.4996	<b>0.4514</b>	0.0449	0.0416	0.9109	0.9371	3.46
	$10^9$	0.4993	<b>0.4508</b>	0.0450	0.0411	0.9028	0.9143	3.01

Table 3.1: Temporal versus spatial stability, Case G. The model employed here is based on a modified Orr-Sommerfeld equation—rather than a system based on primitive variables as done in the bulk of the paper—which is why the temporal results have slightly larger growth rates  $\omega_i$  than those displayed in Fig. 3.2; this is related to the need of computing numerically  $d^2U/dy^2$  and  $dC_d/dy$  in the Orr-Sommerfeld-like equation. In italics, the growth rates obtained from Gaster's transformation are reported; the parameters imposed in each simulation are indicated with bold characters. The solutions for  $Re = 10^9$  coincide with those found using the inviscid equations.

The amplitude of the sensitivity functions,  $|G_U(y)|$  and  $|G_{C_d}(y)|$ , in the spatial and temporal stability frameworks is of same order of magnitude (not shown here) since they are related through temporal spatial the complex group velocity  $C_g$ . It is found that

$|G_U^{temporal}| \approx |C_g| |G_U^{spatial}|$  with  $|C_g| \approx c_g \approx 1$  in the present case. Obtaining and comparing results in the temporal and spatial stability frameworks, such as in Table I, is a good means to validate the sensitivity functions and to verify the accuracy of the computations of the adjoint stability equations.

## APPENDIX C: correction to compare continuous and discrete adjoint eigenfunctions

The discretization operation transform the operator  $\mathcal{L}$  into a matrix  $\mathbf{A}$  and of course do the same things to the unknown functions that becomes vectors.

continuous	discrete
$\mathcal{L}$	$\mathbf{A}$
$q$	$\hat{q}$

This has a serious and most often hidden repercussion in th approach to solve the adjoint equations.

As above stated the derivation of the adjoint equation start with the enforcing of the Lagrange identity:

$$\langle q; \mathcal{L}q \rangle = \langle \mathcal{L}^\dagger q^\dagger; q \rangle \quad (3.14)$$

where the scalar product  $\langle ; \rangle$  is defined in our case as:

$$\langle a; b \rangle = \int_0^{y_\infty} \bar{a} \cdot b dy \approx \sum_{i=1}^N \sum_{j=1}^N \hat{a}_i^T w_{i,j} \hat{b}_j = \hat{\mathbf{a}}^T \mathbf{M} \hat{\mathbf{b}} = \langle a; b \rangle_{\mathbf{M}} \quad (3.15)$$

Is it clear from equation 3.15 that the scalar product takes two different forms in the continuous and in the discrete case. In fact in the discrete case is mandatory to introduce the quadrature rule weights  $w_{i,j}$  of the chosen discretization.  $\mathbf{M}$  is the matrix representation of the weights and is symmetric and positive defined.

In order to compute and solve the adjoint equation one could proceed as follow:

- The direct problem is defined in the continuous space as  $\mathcal{L}q = 0$
- Chose a discretization (FEM, FD, Chebychev polynomials...) and transform the above problem in a discrete one  $\mathbf{A}\hat{q}$
- Solve it to obtain the discrete version of the eigenfunctions  $\hat{q}$

For the adjoint problem on should at first compute the adjoint operator, this can be done using the Lagrangian identity at a continuous level:

$$\begin{aligned} \langle q; \mathcal{L}q \rangle &= \langle \mathcal{L}^\dagger q^\dagger; q \rangle \\ \Rightarrow \int_0^{y_\infty} \overline{q^\dagger} \mathcal{L}q dy &= \int_0^{y_\infty} \overline{\mathcal{L}^\dagger q^\dagger} q dy \end{aligned} \quad (3.16)$$

From the last equation starting from the left part is it possible after some manipulation to retrieve the form on the right part and so find the formulation of the adjoint operator.

It is important to pinpoint that in the above equation the scalar product  $\langle a; b \rangle$  is enforced at a continuous level.

And now to solve the adjoint system the procedure 3.5 can be used changing the direct system with the adjoint one. The above way of computing the adjoint and solve the system is called **continuous approach**.

To summarize this approach one can straight forward solve the direct problem computationally, mathematically find the adjoint operator using the continuous scalar product and the Lagrange identity and then discretize the adjoint problem and solve it computationally. This is why the **continuous approach** is sometimes known as derive than discretize. And the stability and accuracy problems derive directly from the fact that we discretize the problem two times (the direct first and than the adjoint).

On the contrary in the **discrete approach** the scalar product 3.15 is enforced at the discrete level in order to use the already discretized direct equation to retrive the adjoint system at a discrete level, to limit the computational errors.

$$\begin{aligned} \langle q^\dagger; \mathcal{L}q \rangle &= \langle \mathcal{L}^\dagger q^\dagger; q \rangle \\ \Rightarrow \overline{\hat{q}^\dagger}^T \mathbf{M} \mathbf{A} \hat{q} &= (\overline{\mathbf{A}^\dagger \hat{q}^\dagger})^T \mathbf{M} \hat{q} \\ \Rightarrow \mathbf{M} \mathbf{A} &= \overline{\mathbf{A}^\dagger}^T \mathbf{M} \\ \Rightarrow \mathbf{A}^\dagger &= \mathbf{M}^{-1} \overline{\mathbf{A}}^T \mathbf{M} \end{aligned} \quad (3.17)$$

## Chapter 4

# Effect of geometrical parameters and inertia on the apparent permeability tensor in fibrous porous media

### 4.1 Introduction

The flow through porous media is a problem of importance for several natural and technological applications. Since Darcy's original formulation [26], which relates the flow rate through a porous bed to the pressure drop across the bed's sides, many corrections have been made to account, for example, for viscous effects [17] or for the consequences of inertia [32]. All of the cited works are of empirical nature, but homogenisation has been able to recover all of these formulations rigorously starting from the Navier-Stokes equations [70]. This latter approach is sometimes defined VANS, for Volume-Averaged Navier-Stokes.

The theory requires the knowledge of a number of terms, most notably, in the case of an isotropic porous bed, a permeability coefficient and a Forchheimer coefficient. Initial efforts in defining these terms were based on a combination of physical reasoning and measurements, leading to expressions known as the Kozeny-Carman [46, 22] and the Ergun [29] correlations. The first provides the permeability for the laminar flow of a single-phase fluid through a packed bed of sand grains, as function of the porosity and the diameter of the grains, while the second extends Darcy's law to let the pressure drop depend on two terms, one proportional to the velocity and the second to its square, thus accounting for inertia. These approaches do not consider microstructural or geometrical features of the porous bed, which can render the permeability a tensorial quantity, and are often restricted to simple unidirectional flows. In the present work we are concerned with a transversely isotropic material composed by parallel fibers of circular cross-section, with one axis of symmetry,

$(O, x_3)$ ; in such materials the permeability is a diagonal tensor with the component in the direction parallel to the fibers greater than those along the transverse axes. For such an arrangement we will investigate the effects of both the direction of the forcing pressure gradient and inertia. When the latter effect is present, embodied by a Reynolds number  $Re_d$ , based on mean velocity through the medium and fibers' diameter, exceeding an order one threshold, the permeability is no more simply defined upon geometrical properties. This new permeability, which arises from a well-defined closure problem, is then called *apparent permeability*.

The influence of the geometry of the solid inclusions has been addressed previously by Yazdchi et al. [71] for arrays of cylinders in both square and hexagonal (or staggered) patterns, with the cylinders' section which can vary in shape. The results, in the two-dimensional and low Reynolds number limits, demonstrate the dependence of the permeability component along the flow direction to both the porosity and the direction of the macroscopic pressure gradient. The direction of the pressure gradient is found to have a weak effect for beds of medium-high porosity ( $\varepsilon > 0.7$ ) and a stronger dependence appears upon the geometry of the solid inclusions.

The influence of the Reynolds number on the permeability and on the Forchheimer correction has been presented in a number of papers. One of the contributions most relevant here is due to Edwards et al. [28]. These authors show that, for arrays of fibers, the apparent permeability decreases with the increase of the Reynolds number, and the rate of this decrease depends on the geometry of the array; also, the Reynolds number is found to have a stronger influence on the apparent permeability when the medium is highly porous. The results of the work by Edwards et al. [28] agree with those by Zampogna and Bottaro [72] and with our own work (as shown later), all for the case of cylindrical fibers, although some issues remain on the persistence of steady solutions in the simulations by Edwards et al. [28] in cases for which a limit cycle should have set in. A fully three-dimensional porous medium, more complex than those discussed so far, has been considered by Soulaine and Quintard [65], confirming the decreasing trend of the apparent permeability with the Reynolds number.

Another contribution which deserves mention is that by Lasseux et al. [48]; they have computed the permeability tensor for various Reynolds numbers, in a two-dimensional geometry with cylinders of square cross-section. Forcing the flow along the main symmetric directions of the fiber, Lasseux et al. [48] have identified different regimes:

- a creeping flow regime for  $0 < Re_d < 10^{-3}$ , without Forchheimer terms;
- a weak inertia regime for  $10^{-3} < Re_d < 1$ , with the Forchheimer correction quadratic in  $Re_d$ ;
- a strong inertia regime for  $1 < Re_d < 10$ , where the Forchheimer correction is linear with the Reynolds number;

- a turbulent regime, for  $Re_d > 10$ , with the Forchheimer correction again quadratic with the Reynolds number.

The boundaries between the different regimes are specific to the geometrical arrangements and to the porosities being considered; a step forward in rendering (some of) these boundaries rigorous and independent of the arrangement of the pores, through the definition of a Reynolds number which accounts for a "topological" coefficient, has been recently made by Pauthenet et al. [59]. For the purposes of the present paper, we must retain that Lasseux et al. [48] have parametrized the Forchheimer correction with the Reynolds number, and have found that the inertial correction is orders of magnitude smaller than the Darcy's term, at least before the turbulent regime sets in. Moreover, Lasseux et al. [48] have studied how a Forchheimer tensor,  $\mathbf{F}$ , depends upon the direction of the macroscopic forcing term with respect to the orientation of the square cross-section of the fibers, for  $Re_d$  up to 30. It is concluded that a deviation angle,  $\gamma$ , exists between the direction of the pressure gradient and that of the mean flow, because of the fibers' geometry. Finally, the inertial correction is strongly influenced by the orientation of the driving pressure gradient, and the tensor  $\mathbf{F}$  is not symmetric (in fact the off-diagonal components are found to be inversely proportional to the diagonal terms, and symmetric with respect to rotations about the diagonal axis of the square, i.e. the direction at  $45^\circ$  in the  $x_1 - x_2$  plane).

The effect of variations in the forcing angle, with restrictions to angles in the  $x_1 - x_2$  plane, is also examined by Soulaine and Quintard [65] with conclusions in qualitative agreement with those of both the contribution just cited and our results described further below. In all cases, the off-diagonal components of the apparent permeability tensor are small and the diagonal components display but a small variation upon rotation of the driving pressure gradient.

As already anticipated, this work investigates how the direction of the macroscopic pressure gradient, the porosity and the Reynolds number can modify the Darcy and Forchheimer closures arising from a VANS model of a fibrous porous medium. We will consider a three-dimensional unit cell for the microscopic model (such a unit cell is sometimes denoted REV, for Representative Elementary Volume), with a generic forcing whose direction is defined by two Euler angles. Given the formidable space of parameters, some representative results are first shown and discussed. Response surfaces in the space of parameters are then identified by the use of a metamodel based on kriging interpolation. For the sake of space, only the first diagonal component of the apparent permeability tensor is discussed in detail in the paper; however, all components have been computed. They represent an extremely useful data base which we are now in the process of using in macroscopic simulations of flows through bundles of fibers of varying orientation and density.

## 4.2 The Volume-Averaged Navier-Stokes (VANS) method

### 4.3 Validation and setup

In this section the numerical methodology, the parameters, the setup and the validation for some reference cases are given.

#### 4.3.1 Computational domain

The geometry used for the base REV is shown in figure 4.1: a cylindrical inclusion is present at the centre of the REV and four quarters of cylinders are situated at the corners. The lateral length of the cubic envelop is  $\ell$ , which is used as length scale for the microscopic problem; the diameter  $d$  of the cylinders is adapted as a function of the desired porosity  $\varepsilon$ , ratio between the fluid volume over the total REV volume ( $\ell^3$ ).

The forcing term  $\mathbf{f}$  of the DNS is a vector whose direction is defined by two Euler angles, with rotations of the form:  $\theta \mathbf{e}_3 + \phi \mathbf{e}_2^I$  (cf. figure 4.1). Its amplitude is set a priori and is connected to the Reynolds number,  $Re_d$ , defined with the mean velocity over the REV and the fiber diameter,  $d$ .  $Re_d$  is a result of the calculations, once the mean velocity is evaluated.

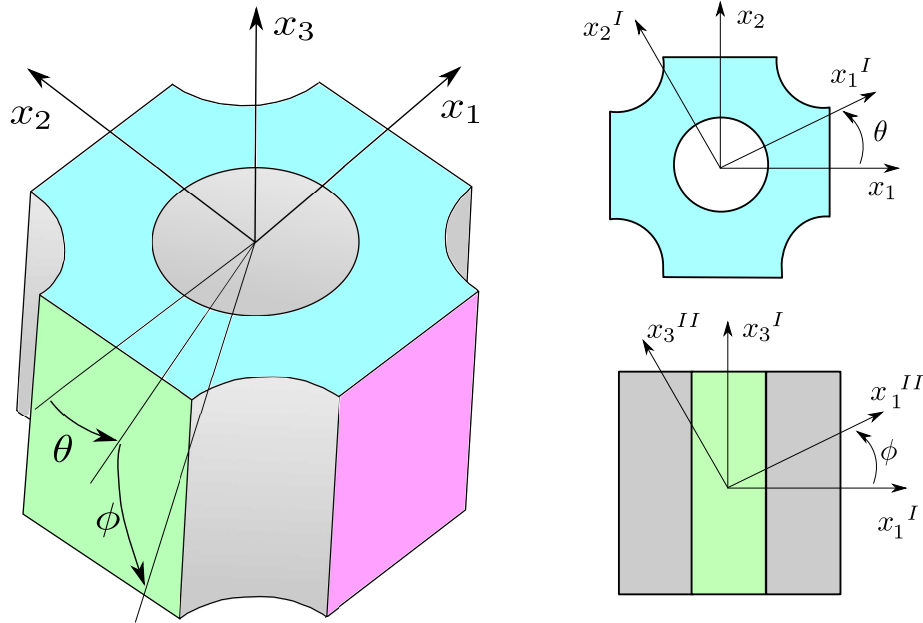


Figure 4.1: REV for the fiber geometry investigated.

### 4.3.2 Numerical setup

The simulations have been carried out with the open-source code OpenFOAM [69], based on a finite volume discretization with a colocated arrangement for the unknowns. The standard solver `icoFoam` (incompressible Navier-Stokes) has been modified in order to include a constant pressure gradient acting as a forcing term  $\mathbf{f}$  in equation (2.8). The coupling between the velocity and the pressure equations is based on the pressure implicit split operator referred to as the PISO algorithm. The time derivative term is discretized using the second order backward Euler scheme and all the spatial terms use a second-order central difference stencil based on Gauss finite volume approach. The velocity system is solved with a preconditioned bi-conjugate gradient (PBiCG) iterative solver with the tolerance on the velocity residuals set to  $10^{-8}$ , associated to a diagonal incomplete lower upper preconditioner (DILU). The pressure equation is solved with a geometric-algebraic multigrid (GAMG) algorithm associated to a Gauss-Seidel smoother and the tolerance on the pressure residuals is here equal to  $10^{-6}$ . Cyclic boundary conditions are applied to all fields on all fluid boundaries along the three directions, and the no-slip condition is imposed on the surface of the solid inclusions. The time step  $\Delta t$  is automatically determined to ensure that the maximum Courant number,  $Co$ , respects the condition:  $Co = \|v_\beta\| \Delta t / \Delta x < 1/2$ , in which  $\|v_\beta\|$  is the local velocity magnitude in the REV and  $\Delta x$  is the local grid spacing.  $Co$  is basically the ratio between the fluid speed and the velocity to propagate information through the mesh and the condition  $Co < 1/2$  is found to be sufficient to have a stable solver.

### 4.3.3 Mesh convergence analysis

The mesh has been computed using the internal OpenFOAM mesher named *snappy-HexMesh*. The final grid is mainly composed by hexahedral cells with a refined regular grid in the boundary layer regions next to the solid surfaces. Three different mesh sizes, with  $0.65 \times 10^6$ ,  $10^6$  and  $1.5 \times 10^6$  elements, have been tested in order to demonstrate spatial convergence. This has been assessed using the Grid Convergence Index (*GCI*) introduced by Roache [62].

Details of the coarsest mesh used are shown in figure 4.2. On the right frame a close up of the grid in the neighbourhood of the fiber's boundary is displayed: twenty points are used in the structured portion of the mesh along the wall-normal direction.

The GCI method is based upon a grid refinement error estimator derived from the theory of generalized Richardson extrapolation. It measures the ratio between the computed value of a quantity over the asymptotic numerical value, thus indicating how far the solution is from the asymptotic ("exact") value. The procedure is simple and provides a method to estimate the order of the spatial convergence, based on two or three different grid sizes. First of all, the grids must be generated with the same algorithm and they must have the same final quality. In each simulation a physical scalar quantity representative of

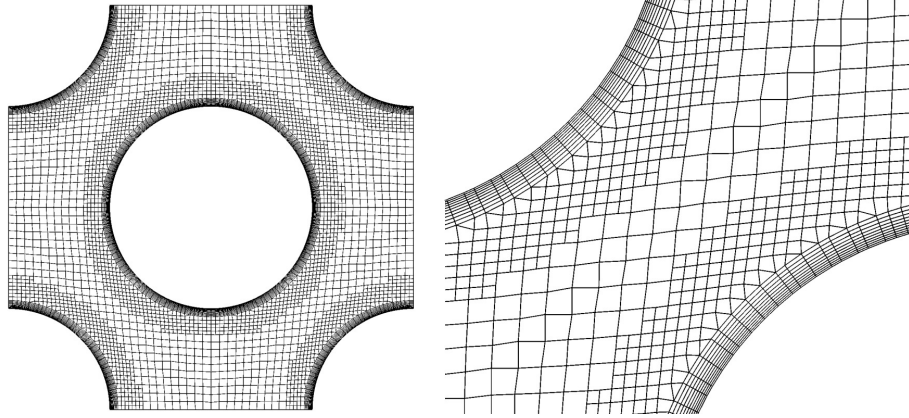


Figure 4.2: Mesh used for the computation; top view (left) and zoom in the boundary layer region (right).  $\varepsilon = 0.6$ .

the physical phenomenon must be sampled. The method follows the following four steps:

1. Estimate the order of convergence of the procedure, defined as  $p = \ln \left( \frac{f_3 - f_2}{f_2 - f_1} \right) / \ln r$ , where  $r$  is the grid refinement ratio between each grid (it is computed as the ratio between the number of elements of two consecutive grids; the approach imposes that  $r$  should remain constant between any couple of consecutive grids and be larger than 1.1), and  $f_i$  represents the quantity of interest in each grid (1=coarse, 2=medium and 3=fine).
2. Compute the relative error between grid  $i$  and  $j$ :  $|\epsilon|_{ij} = \frac{f_j - f_i}{f_i}$ , for  $(i, j) \in \{(1, 2), (2, 3)\}$ .
3. Compute  $GCI_{ij} = \frac{F_s |\epsilon|_{ij}}{r^p - 1}$ , with  $F_s$  a safety factor equal to 1.25 if the grids are three, and equal to 3 if the grids are only two [62].
4. Check whether each grid level yields a solution that is in the asymptotic range of convergence; this means that the quotient  $AC = \frac{GCI_{23}}{GCI_{12}} \frac{1}{r^p}$  should be as close as possible to one.

In our case the quantity of interest chosen is the intrinsic average velocity inside the porous medium, and the results are summarized in table 4.1. From the table it can be seen that the intrinsic velocity difference is very small from one grid to the next and the coarse grid provides results close to the expected asymptotic value. This is taken as a sufficiently convincing argument to carry out all the computations in the following with a grid density equal to that of grid 1.

mesh index	mesh identifier	average velocity REV	metric	value
3	fine	1.11	$GCI_{23}$	0.366%
2	medium	1.07	$GCI_{12}$	1.11%
1	coarse	1.09	AC	1.006

Table 4.1: Convergence analysis. Left: average velocity within the REV, normalized with  $\frac{K_{11}}{\nu_\beta} \|\mathbf{f}\|$ . Right: grid convergence metrics. The REV has  $\varepsilon = 0.6$ , the motion is along  $x_1$ , i.e.  $\theta = \phi = 0$  and  $Re_d \rightarrow 0$ .

#### 4.3.4 Validation on two different configurations

The results published in the literature by Zampogna and Bottaro [72] and Yazdchi et al. [71] are now used to validate both the methodology and our choices of the computational parameters. In the cited papers, three-dimensional computations of the permeability components in different cells geometries are presented.

Figure 4.3 displays the comparison for a cell with a square arrangements of the fibers; here the permeability is evaluated along the two principal directions,  $x_1$  and  $x_3$ . A good agreement is found with the published results. Figure 4.4 shows a similar comparison for a staggered arrangement of the inclusions in the unit cell. In this case the section of the cell is rectangular. The agreement for the only permeability component available in the literature is again satisfactory.

Finally, to check the correct implementation of the closure model (??) it is important to verify the equality (??) between the amplitude  $F^M$  of the macroscopic force and its microscopic counterpart obtained through an integration of the DNS fields over the solid boundaries of the inclusions in the REV. Figure 4.5 shows a plot of the relative error between these two forces, i.e.  $\frac{\|F^M - F^m\|}{\|F^m\|}$ , as function of the Reynolds number. We consider the successful comparison displayed in figure 4.5 as the conclusive demonstration of the validity of the approach described here. We have nonetheless carried out the same verification displayed in figure 4.5 for each one of the simulations described in the following, to our satisfaction.

#### 4.3.5 Tests with larger REV's

Since the Reference Elementary Volume (REV) is the unit cell within the porous medium over which average quantities of the VANS are computed, it is important to choose its dimensions appropriately in the inertial regime for, if the REV is too small, it might be easy to miss crucial features of the wakes. For example, to predict the critical Reynolds number,  $Re_c$ , of the first Hopf bifurcation, a REV containing at least three solid inclusions

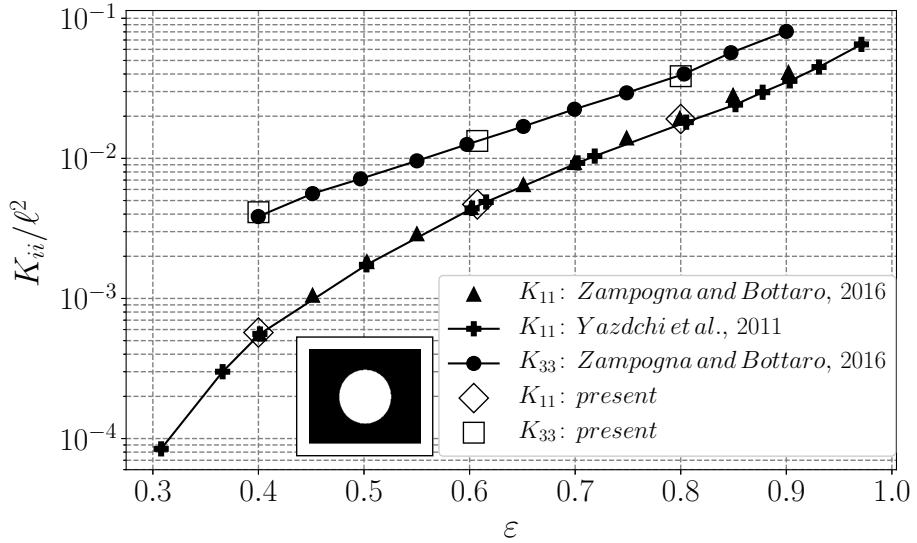


Figure 4.3: Permeability versus porosity for a square arrangement of cylinders. The scaling of the permeability is  $\ell^2$  and is explicitly indicated in the vertical axis.

in the direction of the mean pressure gradient is necessary in the simulations by Agnaou et al. [3]. Among the results reported, it is found that, for a fixed REV size, the error committed in the evaluation of the critical Reynolds number increases with the porosity. This same error is considerably reduced when the mean pressure gradient angle is  $\theta = 45^\circ$ . Thus, the choice of the number of inclusions in a REV is a task not to be overlooked, and the final choice must account for the porosity, the direction of the pressure gradient and the microscopic Reynolds number.

Here, the influence of the numbers of inclusions present in a REV is assessed by focussing only on the velocity components after averaging over the REV. The unit cubic cell of side  $\ell$  is used as reference: starting from this, two additional REV's are built, as shown in figure 4.6. The first one is doubled in both the  $x_1$  and  $x_2$  directions and the case tested numerically is characterised by  $\theta = 0$ ,  $\phi = 0$  (i.e. the forcing pressure gradient is directed along  $x_1$ ), porosity  $\varepsilon = 0.6$  and  $Re_d = 50$ . The second REV configuration is a composition of 3 reference REVs on top of one another along  $x_3$ , with the parameters set to  $\theta = 45^\circ$ ,  $\phi = 45^\circ$ ,  $\varepsilon = 0.6$  and  $Re_d = 100$ .

For both these test cases, no appreciable differences, neither in the mean velocity nor in the forces on the fibers, have been observed, with relative errors on the mean velocity with respect to the reference case which remain below 2%. We take this as sufficient evidence to use, in the following, only the reference cubic REV of side equal to  $\ell$ , with the understanding that only configurations with  $Re_d$  up to around 100 can be considered.

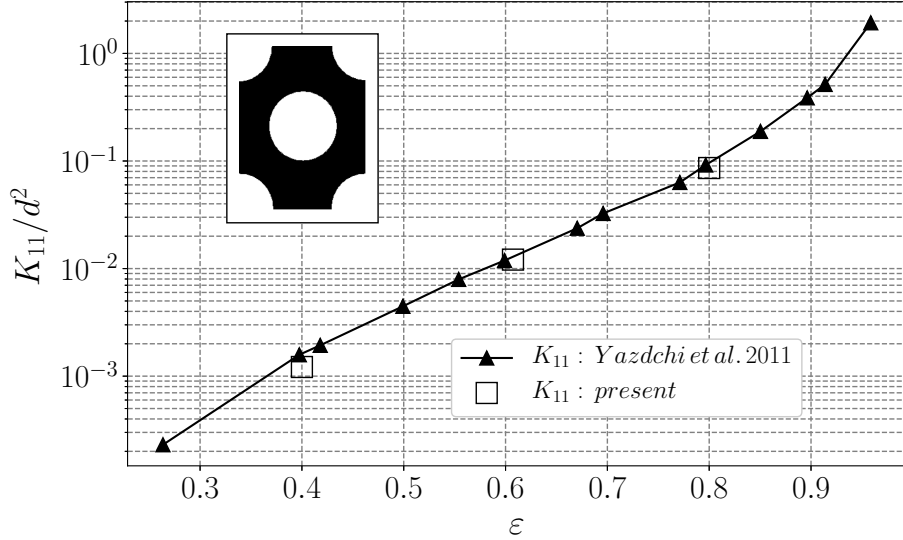


Figure 4.4: Permeability versus porosity for a staggered arrangement of cylinders. The permeability component is here scaled with  $d^2$  (and not  $\ell^2$ ), with  $d$  the diameter of the inclusions.

#### 4.4 Microscopic solutions

In this section, some local microscopic fields computed with direct numerical simulations are shown, together with components of the intermediate tensor  $\mathbf{M}$  coming from the numerical solution of the closure equations (??).

In figure 4.7 (top row) the local  $x_1$  velocity component is drawn for the two-dimensional flow when  $\varepsilon = 0.6$ , for three Reynolds numbers, to cover the transition from the Stokes to the inertial regime. In all plots, the velocities are rendered non-dimensional by the corresponding value of  $\frac{K_{11}}{\nu_\beta} \|\mathbf{f}\|$ . When inertia is absent, the flow has a central symmetry; by increasing the Reynolds number, only the symmetry with respect to the  $x_1$  axis is maintained ( $x_1$  is the direction of the forcing pressure gradient), with the wake's length which increases with  $Re_d$ . When  $Re_d$  is of order 100 the wake spreads to the downstream boundary of the REV, re-entering, because of periodicity, at the upstream side. This  $Re_d$  represents the upper limit of validity for the cubic unit cell of side  $\ell$ ; larger values of  $Re_d$  could only be investigated with longer/larger/thicker REV's.

The non-dimensional local  $M_{11}$  fields for the same parameters are displayed in figure 4.7 (mid row). All values in the figures arise from scaling  $\mathbf{M}$  with  $\ell^2$ . Visually, these local fields are strongly correlated to the local streamwise velocity component in the whole  $Re_d$  range. This is not unexpected since the local velocity drives the convective term of system

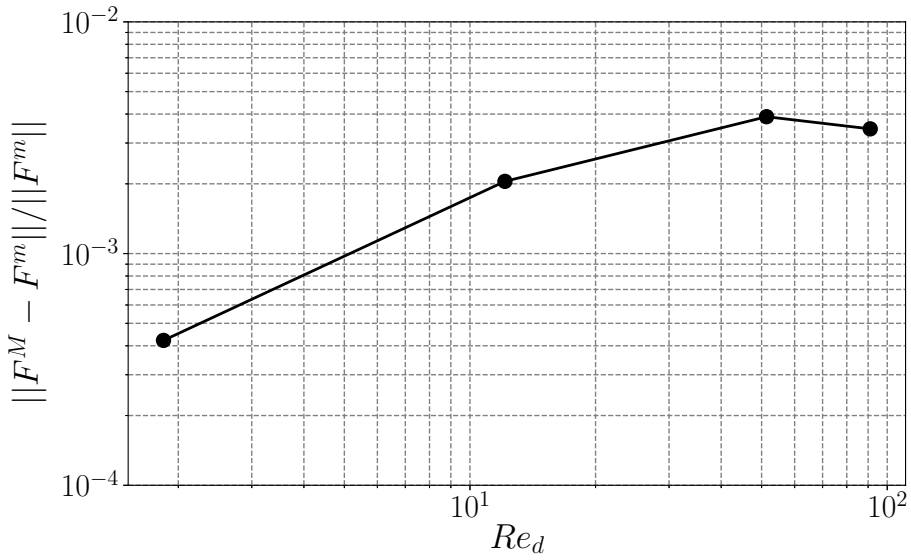


Figure 4.5: Relative error between the microscopically computed forces along the  $x_1$  direction and those arising from the Darcy-Forcheim model;  $\varepsilon = 0.8$  for the REV in the staggered arrangement of Yazdchi et al. [71].

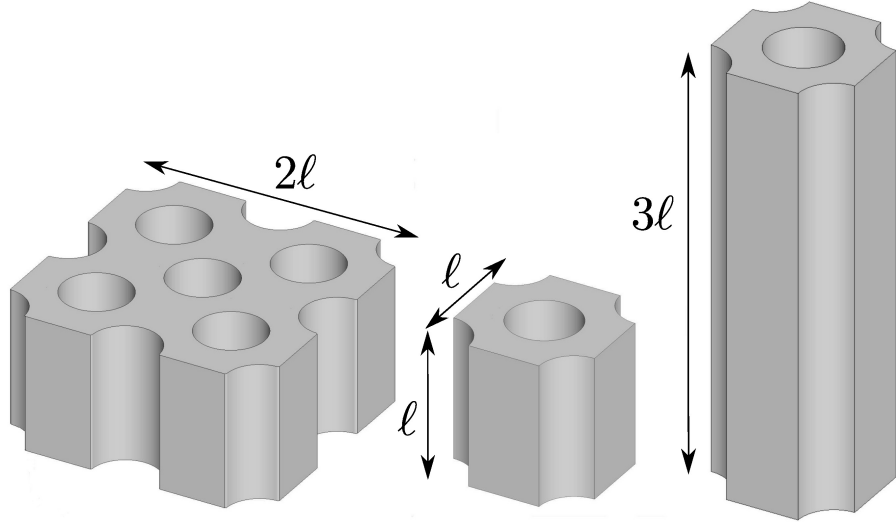


Figure 4.6: REV configurations. Left:  $2 \times 2 \times 1$  arrangement; centre:  $1 \times 1 \times 1$  arrangement (reference); right  $1 \times 1 \times 3$  arrangement.

(??). The central symmetry of all components of  $\mathbf{M}$  in the Stokes regime is coupled to the

rotational invariance of the apparent permeability tensor in two-dimensional flows.

The effect of varying the porosity is shown in figure 4.7 (bottom row) where  $\varepsilon$  is taken equal to 0.4. Even at such a low porosity the stretching of the wake can be noticed, and it increases with  $Re_d$ . Interestingly, this effect is milder when the forcing is inclined by an angle  $\phi$ , since the tighter packing of the inclusions causes a strong deviation of the mean flow along the axis of the fiber. In this case,  $M_{11}$  and  $M_{22}$  behave very similarly to the case  $\phi = 90^\circ$ .

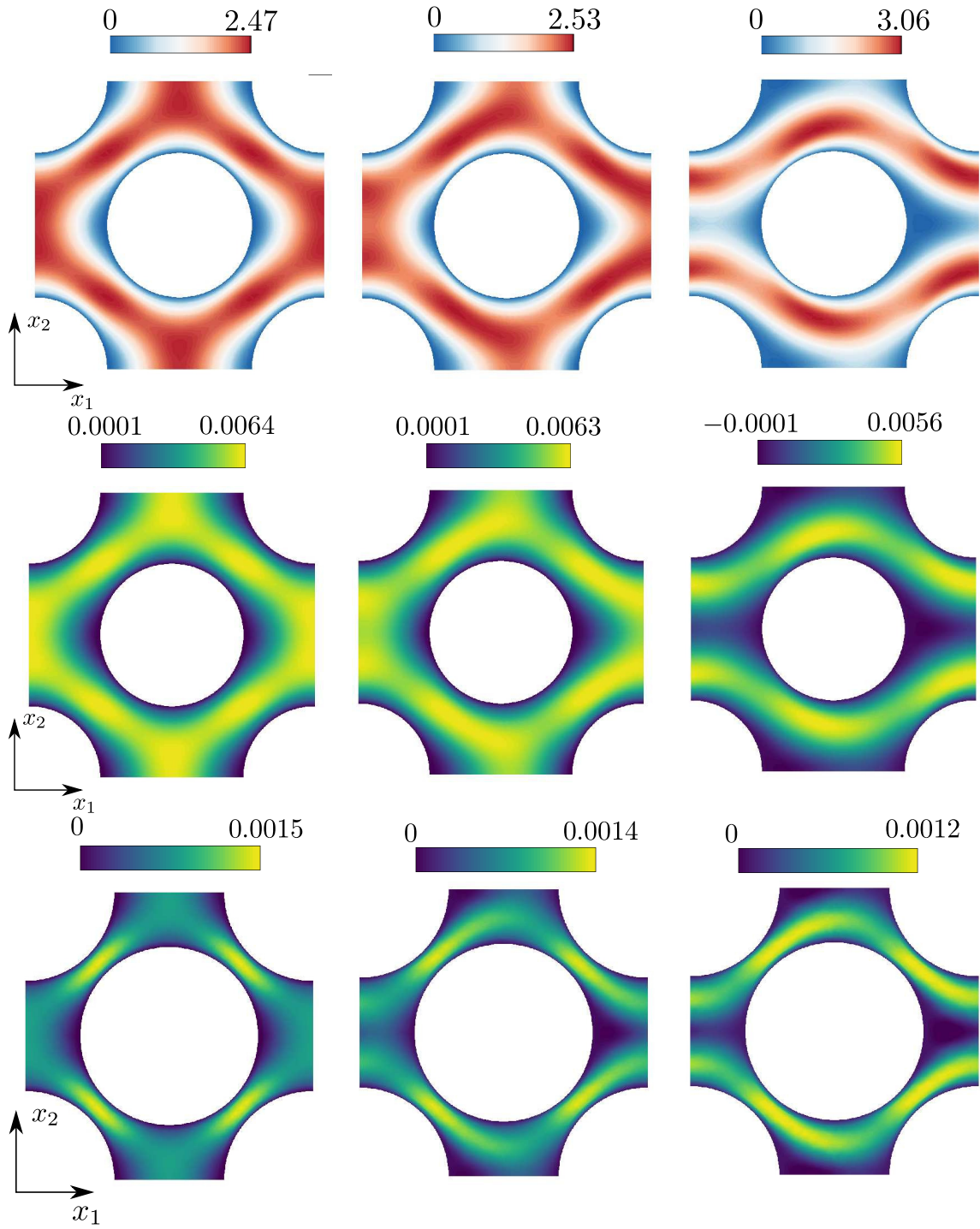


Figure 4.7: Top row: plane view of the dimensionless  $x_1$  component of the local velocity field  $\mathbf{v}_\beta$  for the case  $\theta = 0$ ,  $\phi = 0$ ,  $\varepsilon = 0.6$  and for three Reynolds numbers  $Re_d = 0, 10, 50$ , from left to right. Mid row: microscopic  $M_{15}$  fields corresponding to the images in the top row. Bottom row:  $M_{11}$  fields for the same Euler angles and Reynolds number as in the top two rows, and smaller porosity ( $\varepsilon = 0.4$ ).

Another interesting point emerges by inspection of figure 4.8 where two off-diagonal components of  $\mathbf{M}$  are shown for two porosity values; the first image (left frame) represents a plane flow in the Stokes regime while the second is the plane cut of a three-dimensional solution in the inertial regime. Positive and negative values of the microscopic fields can be seen in both images but, once averaging is applied over the REV, the resulting permeability component is very close to zero (in fact, exactly equal to zero in the Stokes case). This same features occurs for all off-diagonal terms in all cases examined, so that, within the current range of Reynolds numbers, the apparent permeability tensor is, to a good approximation, diagonal<sup>1</sup>.

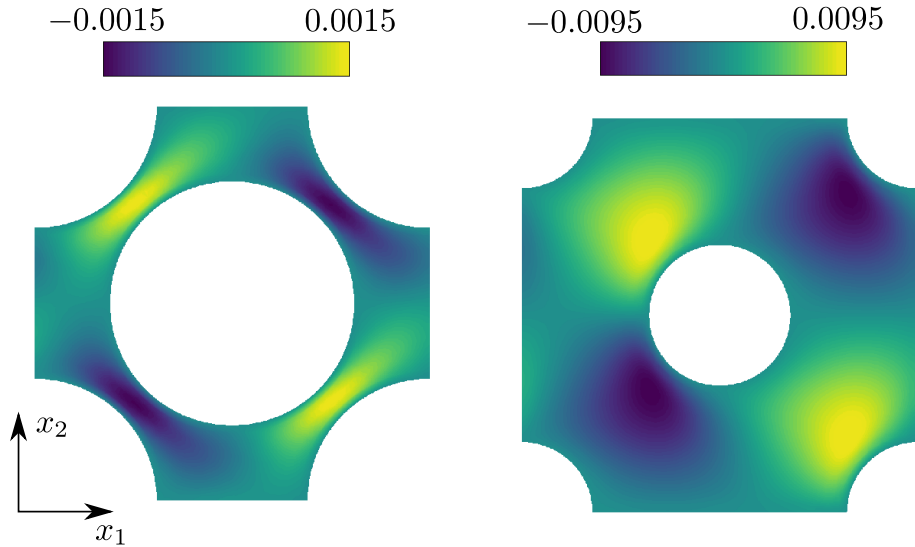


Figure 4.8: right: Non-dimensional  $M_{21}$  field for  $\theta = 0, \phi = 0, Re_d = 10, \varepsilon = 0.8$ , left: Non-dimensional  $M_{12}$  field for  $\theta = 22.5^\circ, \phi = 45^\circ, Re_d = 50, \varepsilon = 0.4$ .

A three-dimensional case is shown in figure 4.9, where all the non-zero terms of the  $\mathbf{M}$  tensor are plotted for a porous structure with  $\varepsilon = 0.6$ . The components shown are  $M_{11}, M_{22}, M_{33}, M_{12}$  and  $M_{21}$ , while  $M_{i3}$  and  $M_{3j}$  are not plotted because they are identically zero to machine accuracy. Distinct features are visible in each image; in particular, in the last frame the  $M_{33}$  microscopic component displays a low wavelength structure along the cylinder's axis. Increasing the dimensions of the REV along  $x_3$  does not alter such a structure, i.e. the  $\ell^3$  domain chosen with its periodic boundary conditions does not filter out significant high wave-numbers of the flow. We further note that the tensor  $\mathbf{M}$  is not symmetric in this case since each off-diagonal component represents the solution of the

---

<sup>1</sup>In fact, there are always at least two orders of magnitude differences between the diagonal and the off-diagonal components. While the latter should not, in principle, be ignored, we will focus attention here only on the dominant terms of the permeability tensor.

closure problem in a specific direction (first index of the field) and the forcing term acts orthogonally to it (second index of the field). Once averaged over the REV it is found that both  $H_{12}$  and  $H_{21}$  are very close to zero.

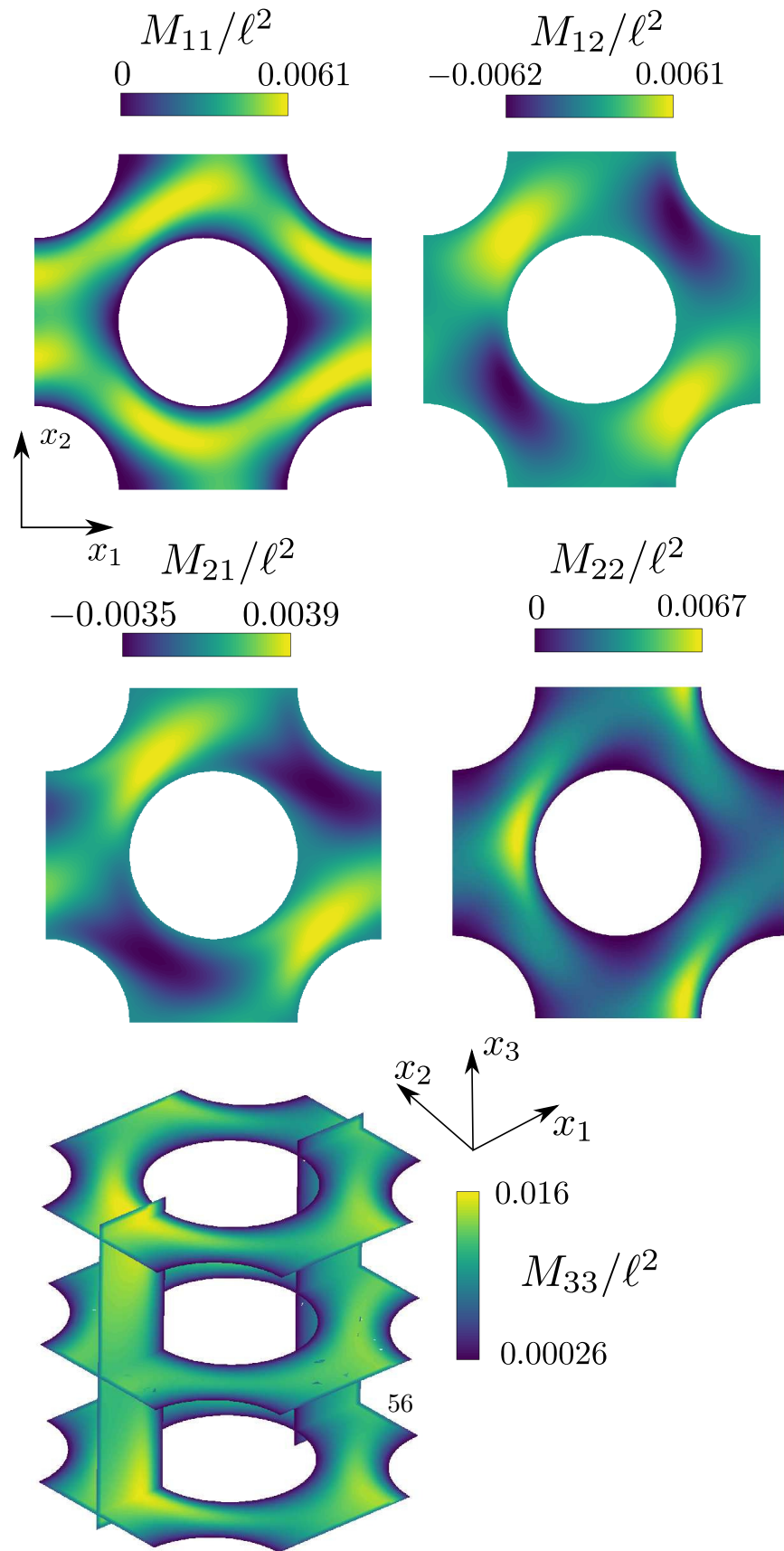


Figure 4.9: Non-dimensional  $\mathbf{M}$  components fields for the case  $\theta = 22.5^\circ, \phi = 45^\circ, Re_d = 50, \varepsilon = 0.6$ .

index	$\theta$	$\phi$	field properties
1	0°	0°	2D symmetric
2	22.5°	0°	2D non-symmetric
3	0°	45°	3D symmetric
4	22.5°	45°	3D non-symmetric
5	–	90°	3D symmetric

Table 4.2: Directions of the forcing tested and property of the solutions.

## 4.5 The apparent permeability tensor

In this section the variations of the diagonal components of the permeability tensor  $\mathbf{H}$  are discussed as function of the direction of the mean forcing, the Reynolds number and the porosity. As stated previously, the Reynolds number ranges from 0 to approximately 100 in order to capture phenomena associated with inertia; the cases considered never lead to unsteady signals. The porosity parameter  $\varepsilon$  is set to either 0.4 (low porosity), 0.6 (medium) or 0.8 (high). The forcing direction is defined by the Euler angles and all the configurations considered in this section are summarized in table 4.2; the choice has been made to explore a reasonably large range of parameters, with both two-dimensional and three-dimensional flows characterized by symmetric and asymmetric patterns.

Let us briefly recall the methodology. First, a DNS is carried out to compute the microscopic flow. Then the closure problem is solved for the tensor  $\mathbf{M}$ . Finally, each component of the apparent permeability  $\mathbf{H}$  is obtained by averaging (equation (2.1)). The results are collected in figures 4.10, 4.11 and 4.12, showing the variation of the diagonal components of  $\mathbf{H}$ .

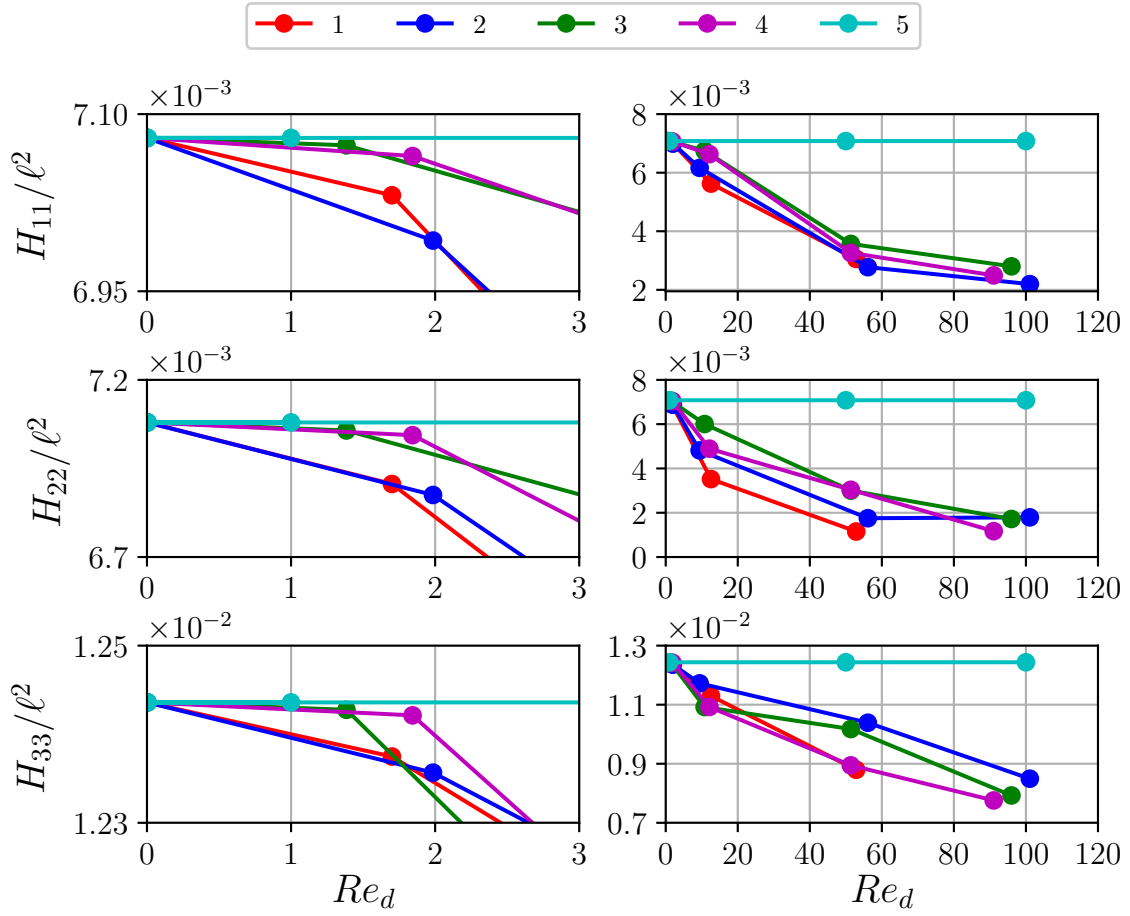


Figure 4.10: Diagonal elements of the apparent permeability  $\mathbf{H}$  as function of the Reynolds number for porosity  $\varepsilon = 0.8$ . The forcing direction is represented through the couple of Euler angles  $(\theta, \phi)$  (cf. table 4.2 for the case index). Left column: low- $Re_d$  regime; right column: inertial regime.

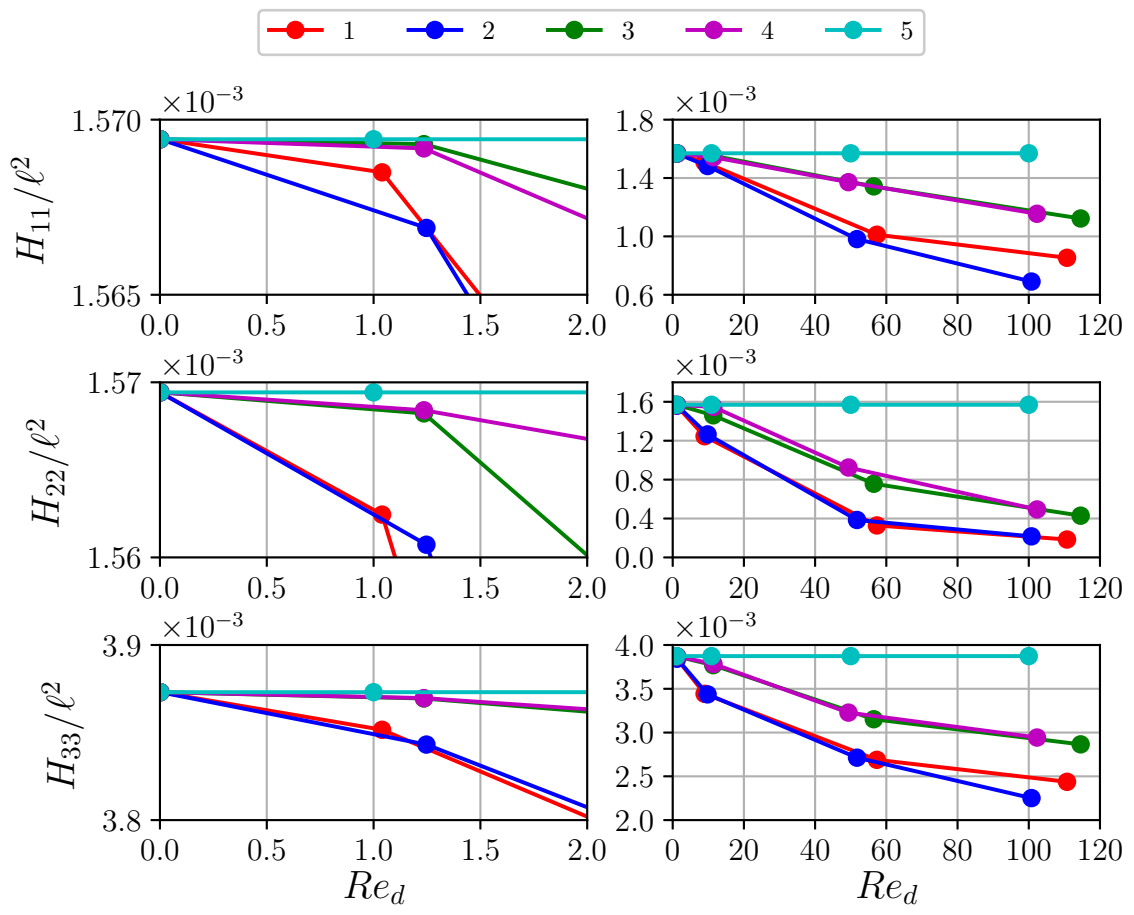


Figure 4.11: Same as figure 4.10 with porosity  $\varepsilon = 0.6$ .

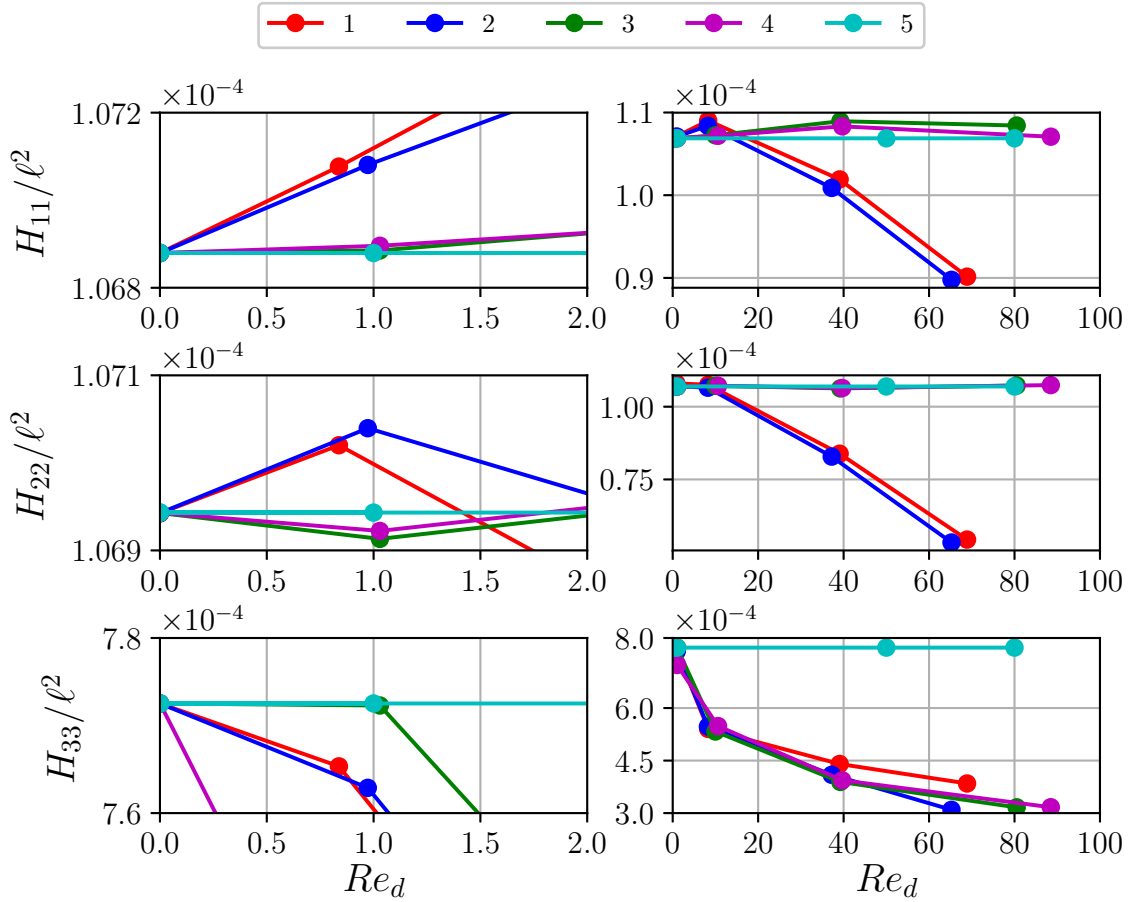


Figure 4.12: Same as figure 4.10 with porosity  $\varepsilon = 0.4$ .

In the left column of each figure we focus on the low- $Re_d$  regime ( $0 < Re_d < 2$ ), while in the right column the effect of inertia can be assessed. As expected, when  $Re_d$  is small the apparent permeability is quasi-Reynolds-number-independent (and can be approximated well by the true permeability). As the Reynolds number increases above a few units, inertial effects grow in importance yielding typically a monotonic decrease of all components of  $\mathbf{H}$ , aside from case indexed 5 ( $\phi = 90^\circ$ ) for which the flow remains aligned with the cylinder's axis. In case 5 the microscopic flow solution is invariant with  $x_3$  and does not change with  $Re_d$  in the range considered, so that  $\mathbf{H}$  is a constant tensor.

When the porosity is large all components show a similar behaviour irrespective of the forcing angle (except, clearly, case 5). Differences start appearing at  $\varepsilon = 0.6$ ; the two cases with  $\phi = 0^\circ$  (index 1 and 2) behave similarly, and so do the two cases indexed 3 and 4 (with  $\phi = 45^\circ$ ). This seems to suggest a weaker effect of  $\theta$  on the permeability components.

For even smaller porosity ( $\varepsilon = 0.4$ ), the blockage which the inclusions cause to the flow produces the unexpected behaviour displayed in figure 4.12. When the flow is purely two-dimensional (cases 1 and 2), variations in the Reynolds number affect  $\mathbf{H}$  significantly; when a pressure gradient along  $x_3$  is present the strong packing of the fibers constrain the fluid to flow prevalently along the fibers' axis, and the apparent permeability is almost  $Re_d$ -independent. When assessing variations in  $H_{jj}$  for this case, attention should also be paid to the fact that the permeability is now at least one order of magnitude smaller than in the previous cases so that variations of the diagonal components shown in figure 4.12 are tiny in absolute terms. This is related to the fact that the inverse of the permeability plays the role of a drag coefficient in the macroscopic expression of the force (cf. equation (??)). In other words, materials with higher porosity (larger space between solid inclusions) offer lower resistance to the motion of the fluid.

Applying the intrinsic average operator to the non-diagonal component of the tensor  $\mathbf{M}$  results in terms that are negligible with respect to their diagonal counterparts, and these results are true for all the parameters considered. This means that there is a very weak coupling between the principal directions of the fiber. The directional decoupling and the diagonal property of the apparent permeability tensor has also been computationally demonstrated on a completely different REV geometry by Soulaine and Quintard [65]. Conversely, Lasseux et al. [48] have carried out a two-dimensional study with fibers of square cross-section, finding that the off-diagonal terms are non-negligible and only about one order of magnitude smaller than the diagonal components. This result is a consequence of the non-rotationally-invariant geometry considered. The present work and the two articles just cited suggest that the diagonal property of the tensor  $\mathbf{H}$  is closely related to the geometry of the porous material, more than to the flow regime.

## 4.6 A metamodel for $\mathbf{H}$

The previous sections has shown how the apparent permeability depends on the two Euler angles, the Reynolds number and the porosity. The space of parameters is formidable and the results found so far are not sufficient to treat, for example, cases characterized by multiple inclusions' sizes and orientations in different regions of the domain, or cases involving a poroelastic medium, with temporally and spatially varying porosity, flow direction and local Reynolds number. The complete solution of the closure problem for a single set of parameters takes approximately 4 CPU hours on our two-processor Intel(r) IVYBRIDGE 2.8Ghz, each with 10 cores and 64 GB of RAM, so that a complete parametric study is, to say the least, unpractical. In view of this, the construction of a metamodel capable to provide a full characterisation of the permeability as a function of all parameters is a worthy endeavor. We have tested several surrogate models, before eventually settling on the kriging approach [45] described in the following.

parameter	values			
$\theta$	0°	22.5°	45°	
$\phi$	0°	22.5°	45°	67.5°
$Re_d$	0	10	50	100
$\varepsilon$	0.4	0.6	0.8	

Table 4.3: Sampling parameters.

#### 4.6.1 DACE sampling

The first step to build a metamodel is the collection of relevant samples. The quality of the final metamodel strongly depends on the samples collected and their number and distribution is of primary importance. The apparent permeability tensor,  $\mathbf{H}$ , depends on four independent variables; the samples have been generated starting from the set of parameters given in table 4.3.

One of the best options to generate the relevant database would be to use a full factorial design approach in which all the combinations of the four variables from table 4.3 are computed. Because of the large number of computations required, this approach has not been retained. We have resorted to the methodology known as DACE (Design and Analysis of Computer Experiments), a technique to fill in the best possible way the space of the parameters of the problem. The Dakota library [2] has been selected for the purpose and the Monte-Carlo incremental random sampling algorithm [38] has been chosen, in order to make efficient use of the cases already computed. This incremental approach selects in a quasi-random way the new samples to generate, starting from the existing ones. In the end, the set of samples comprises 118 cases.

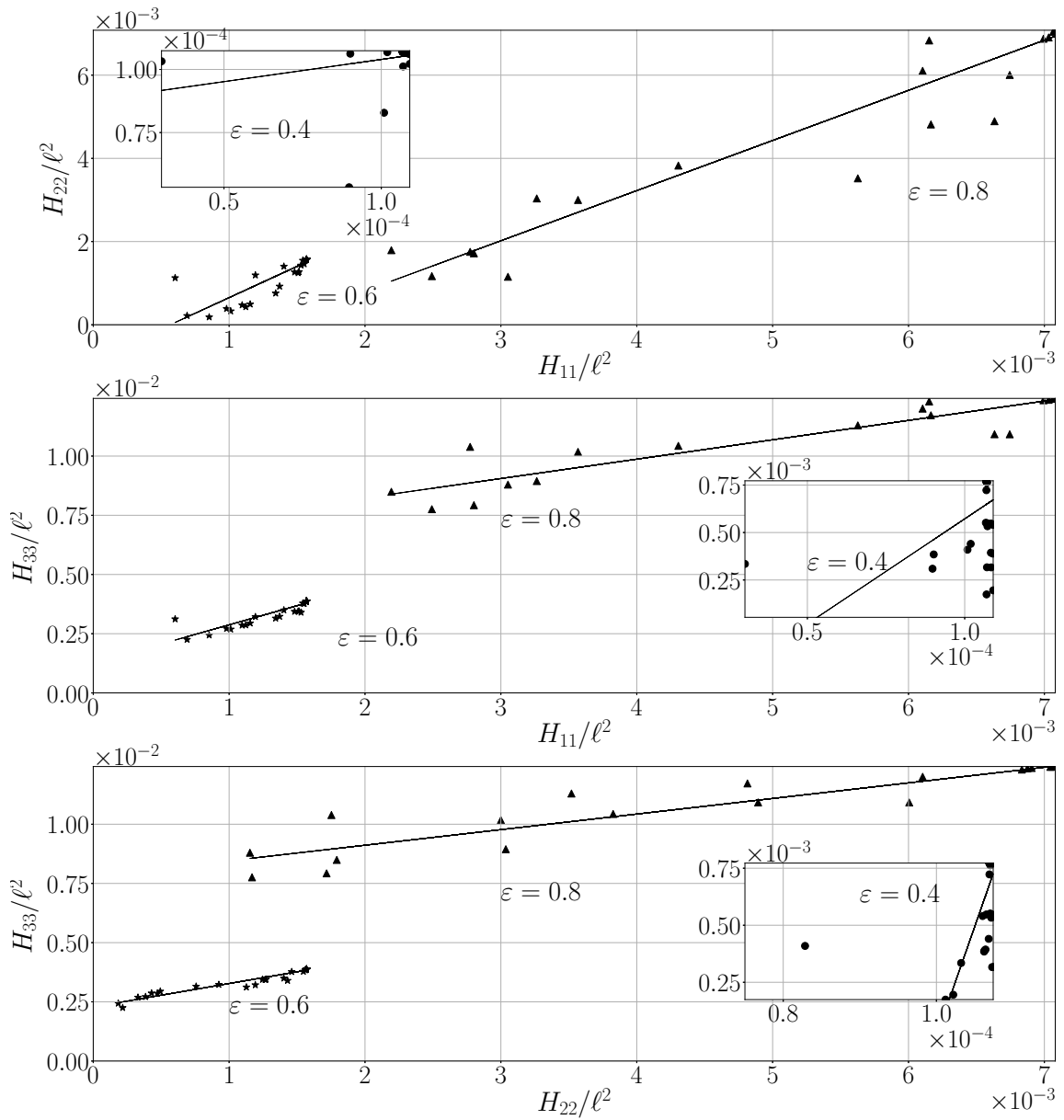


Figure 4.13: Scatter matrix plot for the collected numerical data of the apparent permeability tensor.

In the scatter plot of figure 4.13 the three diagonal components of the permeability tensor are shown as function of one another. The three porosities are separately considered in each of the above plot, and the permeability points are represented with their linear

regression on top. This kind of plot is common in statistical analysis to determine if correlations in the data are present. The permeability components show some correlation with the data points which lie reasonably well on a straight line. This result has a physical implication. Remembering the diagonal dominance of the permeability tensor, we have in the low  $Re_d$  limit:

$$\left(\langle u_\beta \rangle^\beta, \langle v_\beta \rangle^\beta, \langle w_\beta \rangle^\beta\right) \sim \left(H_{11} \frac{\partial p}{\partial x_1}, H_{22} \frac{\partial p}{\partial x_2}, H_{33} \frac{\partial p}{\partial x_3}\right). \quad (4.1)$$

It is then possible to compute the angle between the forcing term,  $\nabla p$ , and the average velocity vector, represented in figure 4.14 for the two-dimensional case,  $\phi = 0$ . This is achieved by taking the ratio between the first two components of Darcy's equation, calling  $\gamma$  the flow deviation with respect to the mean forcing. We thus have:

$$\tan(\theta + \gamma) = \frac{H_{22}}{H_{11}} \tan \theta. \quad (4.2)$$

If the ratio between the two permeability components is equal to one, the angle  $\gamma$  vanishes. The correlation between  $H_{11}$  and  $H_{22}$  controls the deviation of the flow in the  $(x_1, x_2)$  plane, and the argument can easily be extended to  $H_{11}/H_{33}$  and  $H_{22}/H_{33}$  for deviation angles in three-dimensions.

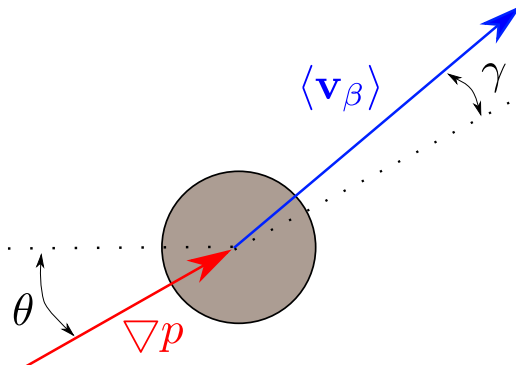


Figure 4.14: Explanatory sketch for the relation between mean pressure gradient and mean velocity field.

Using a linear correlation such as that shown in table 4.4 and figure 4.13, it is observed that in the low porosity case ( $\varepsilon = 0.4$ ) the ratio can become very large indicating a strong deviation of the flow from the forcing direction, because of the strong constraint provided by the inclusions. As the porosity increases, the ratio does not differ much from unity, which means that the deviation remains limited. It is simple to see that the deviation

$\varepsilon$	$H_{11}/H_{22}$	$H_{11}/H_{33}$	$H_{22}/H_{33}$
0.4	1.57	11.06	96.03
0.6	1.50	1.62	0.99
0.8	1.20	0.82	0.66

Table 4.4: Permeability components ratio for three values of the porosity. The permeability ratios here are given by the angular coefficients of the linear correlations displayed in figure 4.13.

angle, for example in the  $(x_1, x_2)$  plane, satisfies the approximate relation

$$\tan \gamma = \frac{\left(1 - \frac{H_{11}}{H_{22}}\right) \tan \theta}{\frac{H_{11}}{H_{22}} + \tan^2 \theta},$$

so that for  $\frac{H_{11}}{H_{22}}$  equal to, say, 1.5, the largest deviation remains always below  $12^\circ$  for any  $\theta$ . It should however be kept in mind that trends based on these ratios are valid only as long as Darcy's law and linear correlations are acceptable. Cases exists for which such trends are violated; for example, a flow with  $\theta = 45^\circ$  and  $\phi = 0^\circ$  has deviation angle  $\gamma$  equal to zero, for whatever porosity. In this case  $H_{11}/H_{22}$  is equal to one and such a point is an outlier in the regression plots of figure 4.13.

#### 4.6.2 Kriging interpolation method

The kriging approach is a linear interpolation/extrapolation method that aims to build a predictor field based on a set of observations  $(\mathbf{x}_i, y(\mathbf{x}_i))$ , for  $i = 1, \dots, n$ .

The predictor  $\hat{f}(\mathbf{x})$  is a sum of a trend function  $t(\mathbf{x})$  and a Gaussian process error model  $e(\mathbf{x})$ :

$$\hat{f}(\mathbf{x}) = t(\mathbf{x}) + e(\mathbf{x}). \quad (4.3)$$

The aim of the error model is to make adjustments on the trend function so that, for any point of the sampling the predictor is exactly equal to the sample, i.e.  $\hat{f}(\mathbf{x}_i) = y(\mathbf{x}_i)$ . This property represents one of the main qualities of this approach. In addition, when the model parameters are conveniently set, the trend function and the covariance model can take into account both smooth and steep variations in the data set.

The trend function defined here is based on a second order least-square regression, with the coefficients found from the solution of the associated linear system. The Gaussian process error model has zero-mean and its covariance between two generic data-points,  $x_i$  and  $x_j$ , is written as

$$\text{Cov}(y(\mathbf{x}_i), y(\mathbf{x}_j)) = \sigma^2 r(\mathbf{x}_i, \mathbf{x}_j).$$

The coefficient  $\sigma$  is an amplitude parameter and  $r(x^i, x^j)$  is a correlation function, based on the Matérn covariance model that reads:

$$r(\mathbf{x}_i, \mathbf{x}_j) = \frac{2^{1-\nu}}{\Gamma(\nu)} \left( \frac{\sqrt{2\nu}|\mathbf{x}_i - \mathbf{x}_j|}{|\boldsymbol{\lambda}|} \right)^\nu K_\nu \left( \frac{\sqrt{2\nu}|\mathbf{x}_i - \mathbf{x}_j|}{|\boldsymbol{\lambda}|} \right), \quad (4.4)$$

where  $K_\nu(\cdot)$  is a modified Bessel function and  $\Gamma(\cdot)$  is the gamma function. The parameters that can be used to tune the metamodel are the amplitude parameter  $\sigma$ , the exponent  $\nu$  and the scale vector  $\boldsymbol{\lambda}$ . The kriging metamodel outputs can show different behaviours for different selections of the above three parameters and their setting is thus crucial. The amplitude parameter  $\sigma$  is chosen to be equal to 1; larger value lead to steeper gradients and undesirable local extrema around the data points. The vector  $\boldsymbol{\lambda} = (\lambda_\theta, \lambda_\phi, \lambda_{Re_d}, \lambda_\varepsilon)$  is a scaling parameter for the distance  $|\mathbf{x}_i - \mathbf{x}_j|$ . In this study, through systematic variations of the parameters it is found that the choice  $\boldsymbol{\lambda} = (1.2, 1, 1, 1)$  yields acceptable results; in particular, the weight along  $\theta$  is mildly larger than in the other directions in order to obtain smoother metamodel surfaces in this direction. The exponent  $\nu$  controls the covariance function and more especially its gradients. When  $\nu = 1/2$  the covariance can be approximated by a negative exponential,  $\exp(-\alpha x)$  and when  $\nu$  goes to infinity it behaves as  $\exp(-\alpha x^2)$ . In the present study, the best (i.e. smoother) results are obtained for  $\nu$  equal to 1.9. The above parameters have been chosen in order to avoid unphysical or unrealistic behaviour of the apparent permeability such as, for instance, negative values or steep, spurious local maxima/minima. The method above is implemented in OpenTURNS and full details are provided by Baudin et al. [6].

In order to prove the robustness of the metamodel we have performed a procedure called cross-validation. This s

and that the number of points choose for the database are enough

The metamodel provides a scalar function (for each term of the  $\mathbf{H}$  tensor) defined in a four-dimensional space. In each of the following figures two parameters are fixed and the response surface is displayed as function of the remaining two, focussing on the  $H_{11}$  component. The other diagonal components of the apparent permeability tensor behave in a similar fashion and will not be shown for brevity. All the results of the metamodel are, however, available from the authors upon request.

In figure 4.15 the angle  $\phi$  is fixed to zero, and the isolines display  $H_{11}$  as function of the angle  $\theta$  and of the Reynolds number,  $Re_d$ , for three values of porosity. The white square symbols indicate the samples used to build the metamodel. The maximum value of each surface is always found for  $Re_d$  equal to zero and  $H_{11}$  typically decreases with  $Re_d$ , when the porosity is sufficiently large. As seen previously, for a porosity approximately greater or equal to 0.6 the variation of the apparent permeability with the angle  $\theta$  is weak in this two-dimensional configuration. For the lowest porosity studied (left frame) the permeability has very small values and the isolines display an irregular behaviour; this is a feature common to all plots relative to the smaller value of  $\varepsilon$ , signaling that it is probably

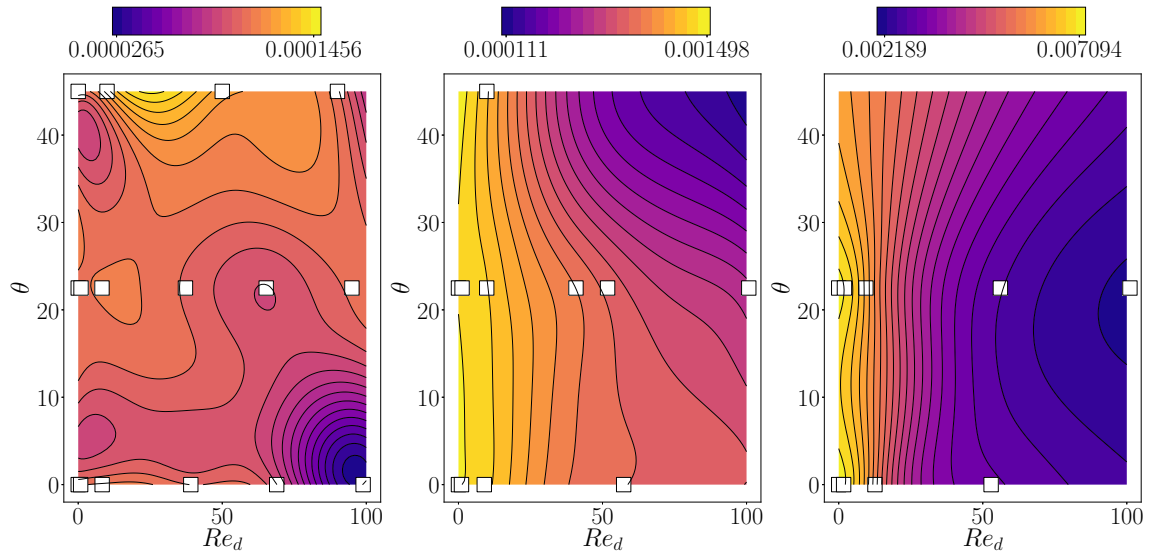


Figure 4.15: Response surfaces of  $H_{11}$  with  $\phi = 0^\circ$  for porosity  $\varepsilon = 0.4, 0.6, 0.8$ , from left to right.

necessary, in this specific case, to insert additional sample points in building the response surfaces.

In figure 4.16 the parameter  $\theta$  is set to  $0^\circ$  and the response surface is displayed in the  $Re_d - \phi$  plane. As already indicated, the results confirm that an increase of the Reynolds number is generally associated to a decrease of the first diagonal component of the apparent permeability tensor. However, the  $H_{11}$  variations with respect to  $\phi$  are more pronounced than those found with respect to  $\theta$  and are due to a real three-dimensionalization of the flow. This conclusion remains to be verified in the lower porosity case (left frame) where the variations are very tiny and more irregular.

In figure 4.17 the Reynolds number is set to the inertial range value of 40 and the response surface is displayed in the  $\theta - \phi$  plane. For the two highest porosity values, 0.6 and 0.8, the results confirm that  $H_{11}$  has a much stronger dependence on  $\phi$  than on  $\theta$ , suggesting that the real test of permeability models must include three-dimensional effects. As seen earlier, the behaviour of the permeability when the porosity is low (left frame in the figure) is not intuitive, with a significant effect of the angle  $\phi$  and a minor influence of  $\theta$ . Again this occurs from the constraint provided to the flow by the inclusions, and from the occurrence of a large deviation  $\gamma$  in these cases.

The response surface is shown in the  $Re_d - \varepsilon$  plane of figure 4.18 for three sets of  $\theta - \phi$  angles. Here a significant effect of the porosity with respect to the Reynolds number is observable. In fact the surface gradient is almost aligned with the porosity direction, i.e. a quasi-Reynolds independence is demonstrated in this plane, and the apparent permeability

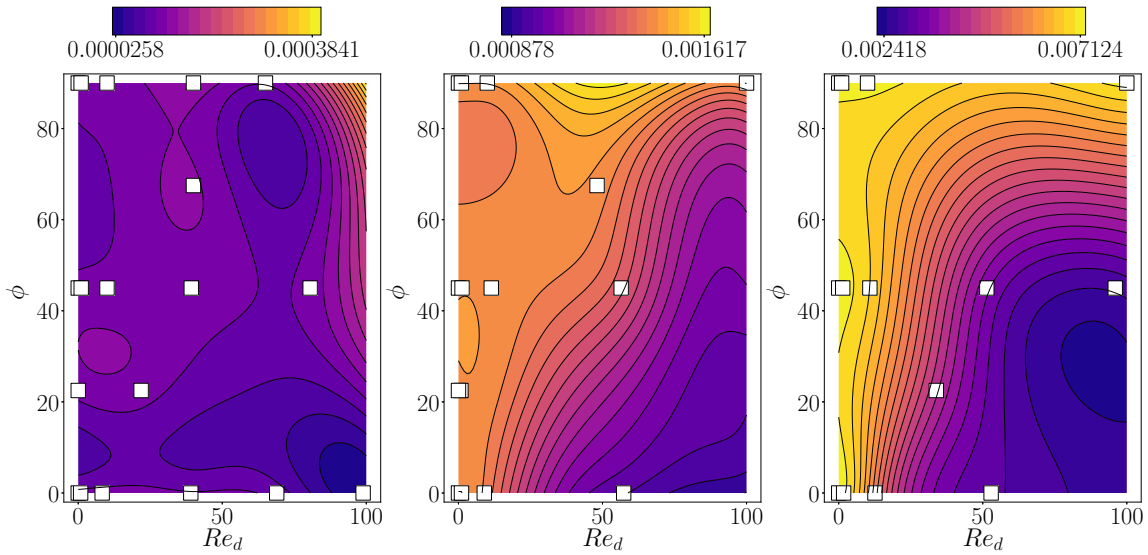


Figure 4.16: Response surfaces of  $H_{11}$  with  $\theta = 0^\circ$  for porosity  $\varepsilon = 0.4, 0.6, 0.8$ , from left to right.

can change by one order of magnitude in the range of the analysed porosity.

Some relatively small Reynolds number effects are visible at porosity equal to 0.8, when the wake of the flow has more space to develop in the inertial regime. In the central figure the flow is aligned with the direction of the fibers and, as expected, it shows practically no dependence with respect to the Reynolds number.

The response surface analysis has confirmed the qualitative trends which had been reached earlier on the basis of a few selected flow cases, yielding at the same time much more detailed information on the behaviour of the apparent permeability with the parameters of the problem. The data base which has been built will be used in future work which will focus, via the VANS approach, on configurations for which neither the porosity nor the local Reynolds number are constant in space or time.

## 4.7 Concluding remarks

The components of the permeability tensor are essential ingredients for any solution of flow through anisotropic porous media. When the flow through the pores resents of significant acceleration effects, the permeability must be modified (it is then called *apparent*) by the presence of a second tensor, the Forchheimer tensor  $\mathbf{F}$ , defined by

$$\mathbf{F} = \mathbf{K}\mathbf{H}^{-1} - \mathbf{I}.$$

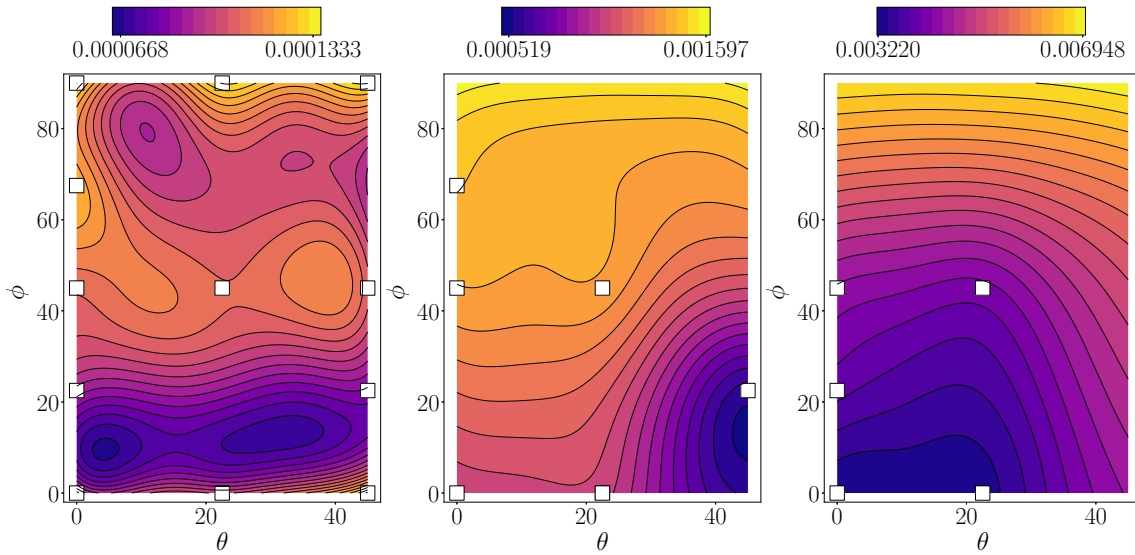


Figure 4.17: Response surfaces of  $H_{11}$  with  $Re = 40$  for porosity  $\varepsilon = 0.4, 0.6, 0.8$ , from left to right.

The permeability,  $\mathbf{K}$ , and the apparent permeability,  $\mathbf{H}$ , can be formally deduced by two closure problems which have been briefly recalled in section 4.2. The real obstacle to the solution of the problem for  $\mathbf{H}$  is the need to know the microscopic velocity fields through the pores. We have solved for such fields in a unit cell (the REV), varying the forcing amplitude and direction, treating over one hundred different cases of flows through arrangements of parallel fibers. From this, we have thus been able to solve the linear system (4.1) for all the unknown elements of the intermediate tensor  $\mathbf{M}$ , from which, through averaging, we have computed the apparent permeability. Such a tensor is indispensable to evaluate accurately the drag force caused by the presence of the fibers, for a macroscopic solution of the flow on the basis of equations [70] when inertial effects are present.

It has been found that the apparent permeability tensor is strongly diagonally dominant for whatever forcing direction and porosity, provided the local Reynolds number remains below a value approximately equal to 100; this results – which is a direct consequence of the transverse isotropy of the material which has been considered here – can be used to compute  $\mathbf{H}$  rapidly, approximating it as a diagonal tensor.

Finally, a metamodel has been used to produce results so as to cover the whole space of parameters, and this has allowed the construction of a complete data base. This data base is now being used in simulations of poroelastic media based on the VANS approach.

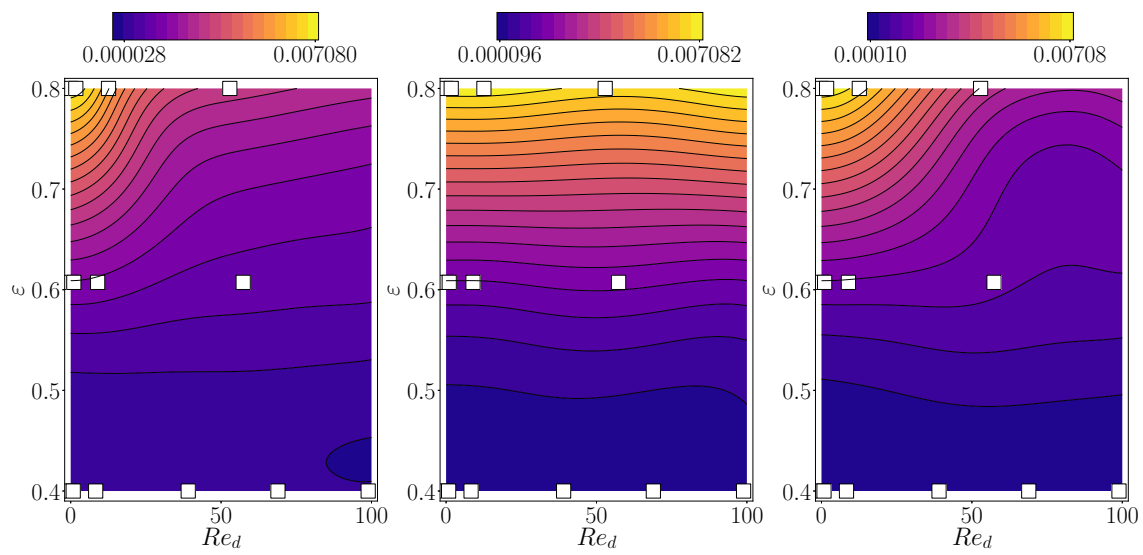


Figure 4.18: Response surface of  $H_{11}$ ; in the left frame  $\phi = \theta = 0$ , in the centre frame  $\phi = 90^\circ$ ,  $\theta = 0$  and on the right  $\phi = 45^\circ$ ,  $\theta = 22.5^\circ$ .

# Bibliography

- [1] JD Ackerman and A Okubo. Reduced mixing in a marine macrophyte canopy. *Functional Ecology*, pages 305–309, 1993.
- [2] B.M. Adams, L.E. Bauman, W.J. Bohnhoff, K.R. Dalbey, M.S. Ebeida, J.P. Eddy, M.S. Eldred, P.D. Hough, K.T. Hu, J.D. Jakeman, J.A. Stephens, L.P. Swiler, D.M. Vigil, , and T.M. Wildey. Dakota, a multilevel parallel object-oriented framework for design optimization, parameter estimation, uncertainty quantification, and sensitivity analysis: Version 6.0 Theory Manual. Technical report, Sandia National Laboratories, SAND2014-4253, 2014.
- [3] Mehrez Agnaou, Didier Lasseux, and Azita Ahmadi. From steady to unsteady laminar flow in model porous structures: an investigation of the first Hopf bifurcation. *Computers & Fluids*, 136:67–82, 2016.
- [4] Philippe Angot, Charles-Henri Bruneau, and Pierre Fabrie. A penalization method to take into account obstacles in incompressible viscous flows. *Numerische Mathematik*, 81(4):497–520, 1999.
- [5] Takashi Asaeda, Takeshi Fujino, and Jagath Manatunge. Morphological adaptations of emergent plants to water flow: a case study with *typha angustifolia*, *zizania latifolia* and *phragmites australis*. *Freshwater Biology*, 50(12):1991–2001, 2005.
- [6] Michaël Baudin, Anne Dutfoy, Bertrand Iooss, and Anne-Laure Popelin. *Open-TURNS: An industrial software for uncertainty quantification in simulation*. Springer International Publishing, Cham, 2016. ISBN 978-3-319-11259-6. doi: 10.1007/978-3-319-11259-6\_64-1. URL [http://dx.doi.org/10.1007/978-3-319-11259-6\\_64-1](http://dx.doi.org/10.1007/978-3-319-11259-6_64-1).
- [7] Gordon S Beavers and Daniel D Joseph. Boundary conditions at a naturally permeable wall. *Journal of fluid mechanics*, 30(1):197–207, 1967.
- [8] Gordon S Beavers and Daniel D Joseph. Boundary conditions at a naturally permeable wall. *Journal of fluid mechanics*, 30(01):197–207, 1967.

- [9] DW Bechert, M Bruse, W Hage, and R Meyer. Biological surfaces and their technological application—laboratory and flight experiments on drag reduction and separation control. *AIAA paper*, 1960, 1997.
- [10] DW Bechert, M Bruse, W vd Hage, JG Th Van der Hoeven, and G Hoppe. Experiments on drag-reducing surfaces and their optimization with an adjustable geometry. *Journal of fluid mechanics*, 338:59–87, 1997.
- [11] S Bhattacharyya and AK Singh. Reduction in drag and vortex shedding frequency through porous sheath around a circular cylinder. *International Journal for Numerical Methods in Fluids*, 65(6):683–698, 2011.
- [12] Bharat Bhushan. *Biomimetics: bioinspired hierarchical-structured surfaces for green science and technology*. Springer, 2016.
- [13] A Boomsma and F Sotiropoulos. Direct numerical simulation of sharkskin denticles in turbulent channel flow. *Physics of Fluids*, 28(3):035106, 2016.
- [14] Alessandro Bottaro, Peter Corbett, and Paolo Luchini. The effect of base flow variation on flow stability. *Journal of Fluid Mechanics*, 476:293–302, 2003.
- [15] WP Breugem, BJ Boersma, and RE Uittenbogaard. The influence of wall permeability on turbulent channel flow. *Journal of Fluid Mechanics*, 562:35–72, 2006.
- [16] W Brevis, M García-Villalba, and Y Niño. Experimental and large eddy simulation study of the flow developed by a sequence of lateral obstacles. *Environmental Fluid Mechanics*, 14(4):873–893, 2014.
- [17] HC Brinkman. A calculation of the viscous force exerted by a flowing fluid on a dense swarm of particles. *Applied Scientific Research*, 1(1):27–34, 1949.
- [18] Charles-Henri Bruneau and Iraj Mortazavi. Passive control of the flow around a square cylinder using porous media. *International Journal for Numerical Methods in Fluids*, 46(4):415–433, 2004.
- [19] Charles-Henri Bruneau and Iraj Mortazavi. Numerical modelling and passive flow control using porous media. *Computers & Fluids*, 37(5):488–498, 2008.
- [20] Charles-Henri Bruneau, Emmanuel Creusé, Delphine Depeyras, Patrick Gilliéron, and Iraj Mortazavi. Coupling active and passive techniques to control the flow past the square back ahmed body. *Computers & Fluids*, 39(10):1875–1892, 2010.
- [21] Dennis M Bushnell, Jerry N Hefner, and Robert L Ash. Effect of compliant wall motion on turbulent boundary layers. *The Physics of Fluids*, 20(10):S31–S48, 1977.

- [22] P. C. Carman. Fluid Flow Through Granular Beds. *Transactions - Institution of Chemical Engineers*, 15:150–166, 1937.
- [23] Peter W Carpenter. Status of transition delay using compliant walls. *Viscous drag reduction in boundary layers*, 123:79–113, 1990.
- [24] Rao Chen, Ikeda Teruaki, Nakata Toshiyuki, and Liu Hao. Owl-inspired leading-edge serrations play a crucial role in aerodynamic force production and sound suppression. *Bioinspiration & Biomimetics*, 12(4):046008, 2017.
- [25] Haecheon Choi, Parviz Moin, and John Kim. Direct numerical simulation of turbulent flow over riblets. *Journal of fluid mechanics*, 255:503–539, 1993.
- [26] Henry Darcy. *Les fontaines publiques de la ville de Dijon*. Victor Dalmont, 1856.
- [27] Brian Dean and Bharat Bhushan. Shark-skin surfaces for fluid-drag reduction in turbulent flow: a review. *Philosophical Transactions of the Royal Society of London A: Mathematical, Physical and Engineering Sciences*, 368(1929):4775–4806, 2010.
- [28] DA Edwards, M Shapiro, P Bar-Yoseph, and M Shapira. The influence of Reynolds number upon the apparent permeability of spatially periodic arrays of cylinders. *Physics of Fluids A: Fluid Dynamics*, 2(1):45–55, 1990.
- [29] Sabri Ergun and Ao Ao Orning. Fluid flow through randomly packed columns and fluidized beds. *Industrial & Engineering Chemistry*, 41(6):1179–1184, 1949.
- [30] Julien Favier, Antoine Dauptain, Davide Basso, and Alessandro Bottaro. Passive separation control using a self-adaptive hairy coating. *Journal of Fluid Mechanics*, 627:451–483, 2009.
- [31] John Finnigan. Turbulence in plant canopies. *Annual review of fluid mechanics*, 32(1):519–571, 2000.
- [32] PH Forchheimer. Wasserbewegung durch boden. *Zeitz. Ver. Duetch Ing.*, 45:1782–1788, 1901.
- [33] Ricardo García-Mayoral and Javier Jiménez. Drag reduction by riblets. *Philosophical Transactions of the Royal Society of London A: Mathematical, Physical and Engineering Sciences*, 369(1940):1412–1427, 2011.
- [34] Ricardo García-Mayoral and Javier Jiménez. Hydrodynamic stability and breakdown of the viscous regime over riblets. *Journal of Fluid Mechanics*, 678:317–347, 2011.
- [35] M Ghisalberti and HM Nepf. The limited growth of vegetated shear layers. *Water Resources Research*, 40(7), 2004.

- [36] Marco Ghisalberti and Heidi Nepf. Mass transport in vegetated shear flows. *Environmental fluid mechanics*, 5(6):527–551, 2005.
- [37] Marco Ghisalberti and Heidi M Nepf. Mixing layers and coherent structures in vegetated aquatic flows. *Journal of Geophysical Research: Oceans*, 107(C2), 2002.
- [38] Anthony A Giunta, Steven F Wojtkiewicz, and Michael S Eldred. Overview of modern design of experiments methods for computational simulations. In *Proceedings of the 41st AIAA aerospace sciences meeting and exhibit, AIAA-2003-0649*, 2003.
- [39] AF Heenan and JF Morrison. Passive control of pressure fluctuations generated by separated flow. *AIAA journal*, 36(6):1014–1022, 1998.
- [40] M Yousuff Hussaini and Thomas A Zang. Spectral methods in fluid dynamics. *Annual review of fluid mechanics*, 19(1):339–367, 1987.
- [41] Motoyuki Itoh, Shinji Tamano, Ryo Iguchi, Kazuhiko Yokota, Norio Akino, Ryutaro Hino, and Shinji Kubo. Turbulent drag reduction by the seal fur surface. *Physics of Fluids*, 18(6):065102, 2006.
- [42] Justin W Jaworski and N Peake. Aerodynamic noise from a poroelastic edge with implications for the silent flight of owls. *Journal of Fluid Mechanics*, 723:456–479, 2013.
- [43] Javier Jimenez, Markus Uhlmann, Alfredo Pinelli, and Genta Kawahara. Turbulent shear flow over active and passive porous surfaces. *Journal of Fluid Mechanics*, 442: 89–117, 2001.
- [44] Katharina Klausmann and Bodo Ruck. Drag reduction of circular cylinders by porous coating on the leeward side. *Journal of Fluid Mechanics*, 813:382–411, 2017.
- [45] Jack P.C. Kleijnen. Regression and kriging metamodels with their experimental designs in simulation: A review. *European Journal of Operational Research*, 256(1):1 – 16, 2017. ISSN 0377-2217. doi: <https://doi.org/10.1016/j.ejor.2016.06.041>.
- [46] J Kozeny. Über grundwasserbewegung. *Wasserkraft und Wasserwirtschaft*, 22(5): 67–70, 1927.
- [47] Amy Lang, Michael T Bradshaw, Jonathon A Smith, Jennifer N Wheelus, Philip Motta, Maria Habegger, and Robert E Hueter. Movable shark scales act as a passive dynamic micro-roughness to control flow separation. *Bioinspiration & Biomimetics*, 9:036017, 07 2014.
- [48] Didier Lasseux, A. Arani Abbasian, and A. Ahmadi. On the stationary macroscopic inertial effects for one phase flow in ordered and disordered porous media. *Physics of Fluids (1994-present)*, 23(7):073103, 2011.

- [49] Michael Le Bars and M Grae Worster. Interfacial conditions between a pure fluid and a porous medium: implications for binary alloy solidification. *Journal of Fluid Mechanics*, 550:149–173, 2006.
- [50] Geoffrey M Lilley. A study of the silent flight of the owl. *AIAA paper*, 2340(1998): 1–6, 1998.
- [51] Paolo Luchini, Fernando Manzo, and Amilcare Pozzi. Resistance of a grooved surface to parallel flow and cross-flow. *Journal of fluid mechanics*, 228:87–109, 1991.
- [52] Samuel Martin and Bharat Bhushan. Discovery of riblets in a bird beak (*rynchops*) for low fluid drag. *Philosophical Transactions of the Royal Society of London A: Mathematical, Physical and Engineering Sciences*, 374(2073), 2016. ISSN 1364-503X. doi: 10.1098/rsta.2016.0134.
- [53] Doug McLean. *Understanding aerodynamics: arguing from the real physics*. John Wiley & Sons, 2012.
- [54] Chiang C Mei and Bogdan Vernescu. *Homogenization methods for multiscale mechanics*. World scientific, 2010.
- [55] Philip Motta, Maria Habegger, Amy Lang, Robert Hueter, and Jessica Davis. Scale morphology and flexibility in the shortfin mako *isurus oxyrinchus* and the blacktip shark *carcharhinus limbatus*. *Journal of morphology*, 273, 10 2012.
- [56] Hiroshi Naito and Koji Fukagata. Numerical simulation of flow around a circular cylinder having porous surface. *Physics of Fluids*, 24(11):117102, 2012.
- [57] Johannes Oeffner and George V. Lauder. The hydrodynamic function of shark skin and two biomimetic applications. *Journal of Experimental Biology*, 215(5):785–795, 2012. ISSN 0022-0949. doi: 10.1242/jeb.063040.
- [58] S Patil and VP Singh. Characteristics of monami wave in submerged vegetated flow. *Journal of Hydrologic Engineering*, 15(3):171–181, 2010.
- [59] M. Pauthenet, Y. Davit, M. Quintard, and A Bottaro. Topological scaling for inertial transition in porous media. *submitted*, 2017.
- [60] Charlotte Py, Emmanuel De Langre, and Bruno Moulia. The mixing layer instability of wind over a flexible crop canopy. *Comptes Rendus Mécanique*, 332(8):613–618, 2004.
- [61] M\_R Raupach, JJ Finnigan, and Y Brunet. Coherent eddies and turbulence in vegetation canopies: the mixing-layer analogy. In *Boundary-Layer Meteorology 25th Anniversary Volume, 1970–1995*, pages 351–382. Springer, 1996.

- [62] P.J. Roache. *Verification and validation in computational science and engineering*. Hermosa Press, Albuquerque, NM., 1998.
- [63] Ravi Singh, MM Bandi, Amala Mahadevan, and Shreyas Mandre. Linear stability analysis for monami in a submerged seagrass bed. *Journal of Fluid Mechanics*, 786, 2016.
- [64] Nathan Slegers, Michael Heilman, Jacob Cranford, Amy Lang, John Yoder, and Maria Laura Habegger. Beneficial aerodynamic effect of wing scales on the climbing flight of butterflies. *Bioinspiration & biomimetics*, 12(1):016013, 2017.
- [65] Cyprien Soulaine and Michel Quintard. On the use of a Darcy–Forchheimer like model for a macro-scale description of turbulence in porous media and its application to structured packings. *International Journal of Heat and Mass Transfer*, 74:88–100, 2014.
- [66] RB Srygley and ALR Thomas. Unconventional lift-generating mechanisms in free-flying butterflies. *Nature*, 420(6916):660, 2002.
- [67] Emmanuel Stratakis, Vassilia Zorba, Marios Barberoglou, Emmanuel Spanakis, Sophia Rhizopoulou, Panagiotis Tzanetakis, Spiros Anastasiadis, and Costas Fotakis. Laser structuring of water-repellent biomimetic surfaces. *SPIE Newsroom*, 10(2.1200901):1441, 2009.
- [68] Cameron Tropea and Horst Bleckmann. *Nature-Inspired Fluid Mechanics: Results of the DFG Priority Programme 1207 "Nature-inspired Fluid Mechanics" 2006-2012*, volume 119. Springer Science & Business Media, 2012.
- [69] H. G. Weller, G. Tabor, H. Jasak, and C. Fureby. A tensorial approach to computational continuum mechanics using object-oriented techniques. *Computers in Physics*, 12(6):620–631, 1998.
- [70] Stephen Whitaker. *The Method of Volume Averaging*, volume 13. Springer Science & Business Media, 2013.
- [71] K Yazdchi, S Srivastava, and S Luding. Microstructural effects on the permeability of periodic fibrous porous media. *International Journal of Multiphase Flow*, 37(8):956–966, 2011.
- [72] G. A. Zampogna and A. Bottaro. Fluid flow over and through a regular bundle of rigid fibres. *Journal of Fluid Mechanics*, 792:5–35, 2016. doi: 10.1017/jfm.2016.66.
- [73] Giuseppe A Zampogna and Alessandro Bottaro. Fluid flow over and through a regular bundle of rigid fibres. *Journal of Fluid Mechanics*, 792:5–35, 2016.

- [74] Giuseppe A Zampogna and Alessandro Bottaro. private communication. *The values of  $\mathcal{K}_{11}$  and  $\mathcal{K}_{22}$  arise from the solution of a local, microscopic problem which accounts for inertia through the porous medium [73]. It is not unexpected that  $\mathcal{K}_{11}$  approaches  $\mathcal{K}_{22}$  as we leave the Stokes regime.*, 2016.
- [75] Giuseppe A Zampogna and Alessandro Bottaro. The pelskin project—part iii: a homogenized model of flows over and through dense poroelastic media. *Meccanica*, 52(8):1797–1808, 2017.
- [76] Giuseppe A Zampogna, Franck Pluvinage, Azeddine Kourta, and Alessandro Bottaro. Instability of canopy flows. *Water Resources Research*, 52(7):5421–5432, 2016.